The Genesis of Mesovortices within a Real-Data Simulation of a Bow Echo System

XIN XU

Key Laboratory of Mesoscale Severe Weather/Ministry of Education, and School of Atmospheric Sciences, Nanjing University, Nanjing, China, and Center for Analysis and Prediction of Storms, University of Oklahoma, Norman, Oklahoma

MING XUE

Key Laboratory of Mesoscale Severe Weather/Ministry of Education, and School of Atmospheric Sciences, Nanjing University, Nanjing, China, and Center for Analysis and Prediction of Storms, and School of Meteorology, University of Oklahoma, Norman, Oklahoma

YUAN WANG

Key Laboratory of Mesoscale Severe Weather/Ministry of Education, and School of Atmospheric Sciences, Nanjing University, Nanjing, China

(Manuscript received 17 July 2014, in final form 8 January 2015)

ABSTRACT

The genesis of two mesovortices (MVs) within a real-data, convection-resolving simulation of the 8 May 2009 central U.S. bow echo system is studied. Both MVs form near the bow apex but differ distinctively in intensity, lifetime, and damage potential. The stronger and longer-lived mesovortex, MVa, stays near the bow apex where the system-scale rear-inflow jet (RIJ) is present. The descending RIJ produces strong downdrafts and surface convergence, which in turn induce strong vertical stretching and intensification of MVa into an intense mesovortex. In contrast, the weaker and shorter-lived mesovortex, MVb, gradually moves away from the bow apex, accompanied by localized convective-scale downdrafts.

Lagrangian circulation and vorticity budget analyses reveal that the vertical vorticity of MVs in general originate from the tilting of near-surface horizontal vorticity, which is mainly created via surface friction. The circulation of the material circuit that ends up to be a horizontal circuit at the foot of the MVs increases as the frictionally generated horizontal vortex tubes pass through the tilted material circuit (tilted following backward trajectories defining the material circuit) surface, especially in the final few minutes prior to mesovortex genesis. The tilted material circuit becomes horizontal at the MV foot, turning associated horizontal vorticity into vertical. The results show at least qualitatively that, in addition to baroclinicity, surface friction can also have significant contributions to the generation of low-level MVs, which was not considered in previous MV studies.

1. Introduction

Severe straight-line winds near the surface, sometimes called derechoes (Johns and Hirt 1987), are often observed in association with quasi-linear convective systems (QLCSs), such as squall lines and bow echoes (Atkins et al. 2004; Wakimoto et al. 2006a). Recent observational and modeling studies show that these damaging near-surface winds are often related to low-level (below 1 km AGL) mesovortices (MVs) within QLCSs (Trapp and Weisman 2003; Atkins et al. 2005; Wheatley et al. 2006). Here, a mesovortex is defined as the meso-γ-scale (Orlanski 1975) circulations forming at low levels on the gust front of QLCSs (Atkins and St. Laurent 2009a). Surface wind damage of Fujita-scale (Fujita 1981) F0 to F1 tornado intensity can be produced through the superposition of the mesovortex vortical flow with strong ambient translational flow (Wakimoto et al. 2006b; Atkins and St. Laurent 2009a). MVs are also known to lead to nonsupercell tornadoes (Forbes and Wakimoto 1983; Funk et al. 1999; Atkins et al. 2005; Schenkman et al. 2012). Tornadic MVs tend to be stronger, deeper, and longer lived in comparison to nontornadic ones (Atkins et al. 2004).

Corresponding author address: Ming Xue, School of Atmospheric Sciences, Nanjing University, No. 163, Qixia Avenue, Nanjing 210093, Jiangsu, China.
E-mail: mxue@ou.edu

DOI: 10.1175/JAS-D-14-0209.1

Considering their damage potential, studying and understanding the genesis processes of MVs are of both theoretical and practical importance. Based on idealized numerical simulations, Trapp and Weisman (2003) proposed that the downward tilting of crosswise horizontal vorticity generated baroclinically along the cold outflow boundary by precipitating downdrafts leads to the formation of a counterrotating vortex pair, and a cyclonic MV forms as the cyclonic member of the pair is enhanced by convergence of planetary vorticity. Based on airborne dual-Doppler radar observations, Wakimoto et al. (2006b) proposed a similar mechanism except that the downdrafts tipping the vortex lines were believed to have been generated mechanically rather than as a result of water loading. The compensating downward motion was driven by the pressure field set up in response to the strong buoyant updrafts. On the contrary, Atkins and St. Laurent (2009b) proposed that the MVs within the 10 June 2003 Saint Louis bow echo formed when baroclinically generated crosswise vorticity was tilted upward by convective updrafts at the gust front. More specifically, it is believed that the subsiding parcels with convective-scale downdrafts or rear-inflow-jet (RIJ; e.g., Smull and Houze 1987; Houze 2004) acquired streamwise horizontal vorticity via baroclinic generation was subsequently tilted into vertical by the updrafts at cold-pool gust front. This uplifting mechanism was also believed to occur within an Oklahoma mesoscale convective system (MCS) by Schenkman et al. (2012) based on a real-data-initialized 400-m grid-spacing simulation.

While the tilting of horizontal vortex lines produces vortex couplets of opposite signs, cyclonic-only MVs had been also observed within QLCSs—for example, within the 24 October 2001 squall-line bow echo (Wheatley and Trapp 2008). The release of horizontal shearing instability was used to explain the formation of cyclonic-only MVs.

Apart from the shearing instability mechanism, previously proposed MV genesis mechanisms have mostly emphasized the importance of baroclinity as the primary source of horizontal vorticity that is tilted into vertical. Indeed, being internal to convective systems, baroclinicity was also found to be critical in the generation of other rotational structures, such as bow echo line-end vortices (Trier et al. 1997; Weisman and Davis 1998; Meng et al. 2012) and mesocyclones (Rotunno and Klemp 1985; Davies-Jones and Brooks 1993; Adlerman et al. 1999; Markowski et al. 2008). However, recent studies have found that surface drag or friction can also be an important source of low-level horizontal vorticity for tornadogenesis. Using a 50-m grid spacing real-data simulation, Schenkman et al. (2014) studied tornadogenesis in the 8 May 2003 Oklahoma City supercell storm and found that at least a significant part of the near-surface vertical vorticity associated with tornadogenesis resulted from reorientation of frictionally (surface drag) generated horizontal vorticity. Impacts of friction on low-level horizontal vorticity were also noticed in the dual-Doppler analysis of the 5 June 2009 Goshen County, Wyoming, supercell (Markowski et al. 2012, their Fig. 3). Nevertheless, the role of friction in the generation of MVs within QCLSs has not been specifically investigated because it had been believed to be unimportant (e.g., Trapp and Weisman 2003).

The 8 May 2009 central U.S. bow echo was a prolific producer of derechoes and tornadoes (Xue et al. 2009). Environmental conditions and the evolution of the bowing system and associated mesoscale convective vortex (MCV) were investigated by Coniglio et al. (2011) and Weisman et al. (2013). Based upon Doppler radar observations, Xu et al. (2015, hereafter XXW15) documented the existence and general behaviors of low-level MVs in this bow echo system. Moreover, a real-data, convection-resolving numerical simulation was also conducted in XXW15 that bears similarity to the observations in many aspects, including the general behaviors of MVs.

Insights into the key factors governing the MV development can help improve the forecasting and warning of severe MVs within the QCLSs. In this study, two of the MVs simulated within the 8 May 2009 bow echo are investigated. Both MVs form near the bow apex but differ distinctively in intensity, lifetime, and damage potential. To study their genesis processes, Lagrangian circulations and vorticity budgets are calculated, and particular attention is paid to the role of surface friction. Circulation analysis along a material circuit can quantify a bulk contribution of baroclinicity and friction from all parcels on the circuit (Markowski et al. 2012), while the detailed evolution of the rotational characteristics of individual parcels requires vorticity budget calculations along individual parcels' trajectories (e.g., Mashiko et al. 2009; Schenkman et al. 2014), which are calculated backward in time starting from a circuit at the "foot" of the MV.

The rest of this paper is organized as follows. Section 2 describes the numerical simulation analyzed in this study. Section 3 first briefly introduces the 8 May 2009 bow echo and then analyzes the evolution of the two MVs of interest. The governing equations of circulation and vorticity are outlined in section 4, with detailed results shown in sections 5 and 6. Further discussions are presented in section 7, and section 8 summarizes and concludes the paper.

2. Numerical experiment setup

The Advanced Research version of the Weather Research and Forecasting Model (ARW; Skamarock et al. 2005) is used to produce the real-data, convection-resolving numerical simulation of the 8 May 2009 bow echo case. The outer domain of the model is configured the same way as the control run (i.e., the arw_cn member) of the real-time storm-scale ensemble forecasts (SSEF; see Xue et al. 2009; Kong et al. 2009) carried out by the Center for Analysis and Prediction of Storms (CAPS), which used a single domain with 4-km grid spacing covering most of the continental United States. However, to better resolve the meso-γ-scale MVs, an inner domain with a 0.8-km grid spacing is added using two-way nesting. This domain is placed in the central United States, having 1441×1081 horizontal grid points. All the analyses in this study are based on the outputs of the fine-resolution 0.8-km domain. The model has 51 levels in the vertical, with the level interval increasing from about 60 m near the surface to about 600 m at the 50-hPa model top.

The outer 4-km domain simulation started at 0000 UTC 8 May 2009, the standard time of the CAPS daily real-time SSEFs. The model initial condition for the 4-km grid was created by assimilating radar and mesoscale surface observations using the Advanced Regional Prediction System (ARPS; Xue et a. 2000) three-dimensional variational data assimilation (3DVAR) cloud analysis system (Xue et al. 2003; Gao et al. 2004) and the operational NCEP North American Mesoscale (NAM) analysis valid at the same time as the background. The model lateral boundary conditions came from the NAM forecasts at 3-h intervals. The inner two-way nested grid was not spawned until 1100 UTC—that is, about 3 h before the genesis of significant MVs within the bowing system—and the nested grid was initialized using the 4-km forecast at that time.

For the model physics, both domains employed the Thompson microphysics scheme (Thompson et al. 2008), Mellor–Yamada–Janjić planetary boundary layer scheme (Janjić 1994), Goddard shortwave radiation scheme (Tao et al. 2003), the Noah (Ek et al. 2003) land surface model (LSM), and the Eta surface layer scheme (Janjić 1996) based on the Monin–Obukhov similarity theory. Readers are referred to Kong et al. (2009) and Xue et al. (2009) for more details on the model configurations.

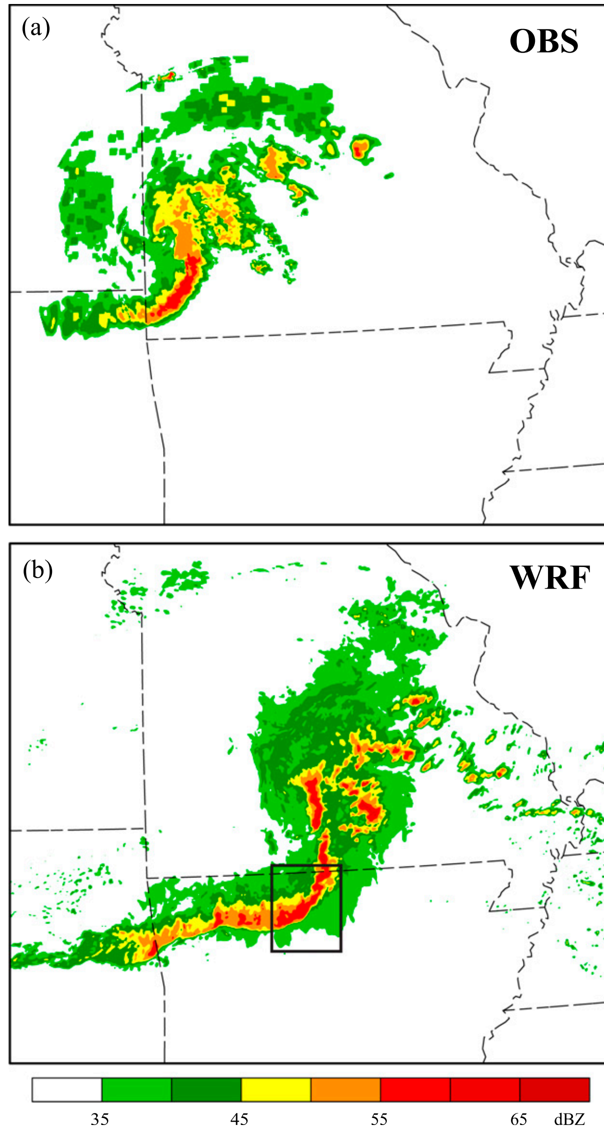

FIG. 1. Composite reflectivity of the 8 May 2009 central U.S. bow echo from (a) radar observation at 1239 UTC and (b) WRF simulation at 1430 UTC. Black box in (b) indicates the domain shown in Fig. 2.

3. The 8 May 2009 central United States bow echo and bow-apex MVs

a. *Case overview*

The mesoscale convective system of interest initially developed from scattered thunderstorms over northeastern Colorado around 0300 UTC on 8 May 2009 (2100 CST on 7 May 2009), which was accompanied by weak synoptic-scale forcing and limited thermodynamic instability within the environment (Coniglio et al. 2011). The initial storms moved southeastward and organized into an MCS in western Kansas by 0700 UTC. A large bow echo developed out of the MCS over southwestern Missouri around 1200 UTC (Fig. 1a). This large bowing system maintained for a couple of hours until about 1800 UTC, during which a number of tornadoes of up to EF-3 intensity on the enhanced Fujita scale (Doswell et al. 2009) and intense derechoes were produced (Xue et al. 2009; Coniglio et al. 2011). A warm-core MCV formed at the northern end of the bow echo, and detailed discussions on this meso-β-scale feature and its role in producing severe surface winds can be found in Weisman et al. (2013) and Evans et al. (2014).

The general evolution of the bow echo is reproduced well by the WRF simulation, in spite of some timing and positioning errors (Fig. 1b). A detailed comparison of the simulation with observations was given in XXW15. Considering that the forecast range is more than 12 h

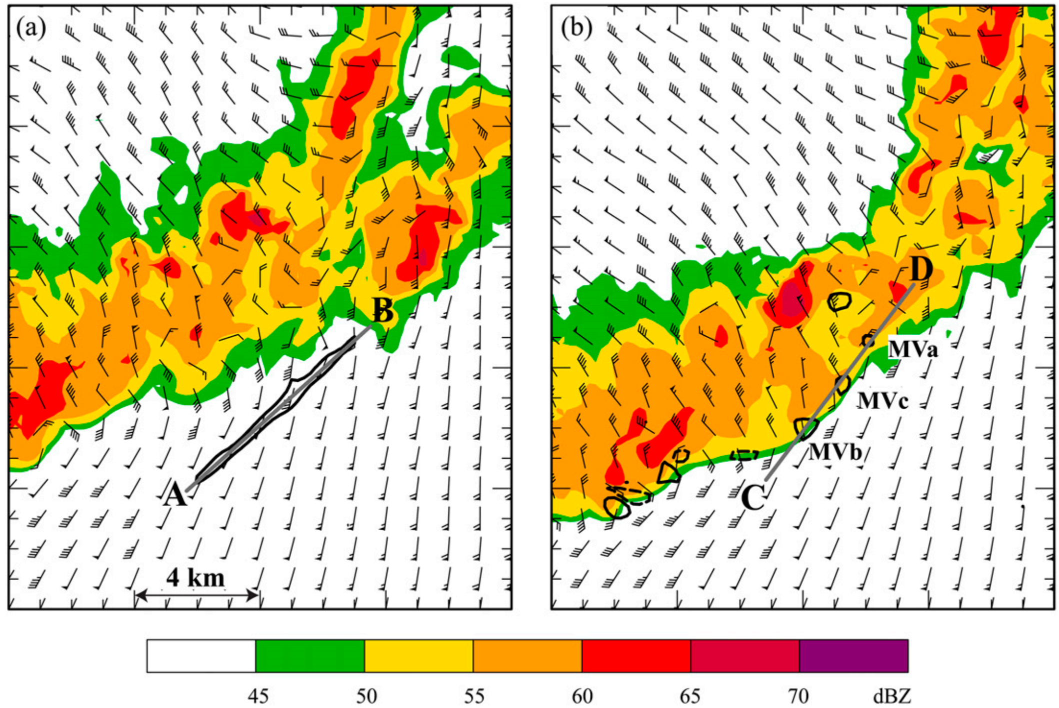

FIG. 2. Composite reflectivity of simulated 8 May 2009 central U.S. bow echo at (a) 1415 UTC and (b) 1425 UTC. Also shown are ground-relative winds at 2.5 km AGL (pennant = 25 m s^{-1}; full barb = 5 m s^{-1}) and vertical vorticity at 200 m AGL (contours). In (a), only the vertical vorticity of 2.5×10^{-3} s^{-1} is plotted; while contours in (b) are for 5.0×10^{-3} s^{-1} (solid) and -5.0×10^{-3} s^{-1} (dashed). Gray straight lines AB and CD mark the positions of vertical cross sections shown in Fig. 3. The plotted domain is indicated in Fig. 1b.

and the convective storms and their organization developed after the initial condition time, and our main interests in this study are with the physical processes rather than the exact prediction, such timing and positioning errors are considered tolerable.

As described in XXW15, a large number of MVs was identified in both observed and simulated bow echo. Although there is no one-to-one correspondence, the observed and simulated MVs share many similarities, as discussed in XXW15, thus providing a basis for the present diagnostic study.

b. Evolution of bow-apex MVs

The two MVs that we focus on in this study developed initially out of an elongated positive vertical vorticity band ahead of the bow apex in the simulation (although the vertical vorticity in this band is not necessarily the main source of vorticity that causes the rapid intensification of the MV vortex at the later stage), which was about 30 km in length and aligned parallel to the leading convective line in the bow echo system (Fig. 2a). Initially, this elongated vertical vorticity band was weak and shallow, possessing weak upward motion (Fig. 3a). However, it deepened and intensified very rapidly when encountering the leading convective line around 1420 UTC (Figs. 2b and 3b), being brought toward the convective line by the preline convergent flow. A mesocyclone developed at this time at 3 km AGL, which was about 5 km in diameter and had 0.02 s^{-1} maximum vertical vorticity, in collocation with a strong rotating updraft of >15 m s^{-1} (not shown). At the lower levels below 1 km AGL, the originally elongated vorticity band evolved into three individual vortices, labeled MVa, MVb, and MVc in Fig. 2b.

MVa, which was labeled MV8 in XXW15, was a strong and long-lived mesovortex, persisting for more than 2 h in the simulation. It developed a high vertical vorticity of 0.053 s^{-1} at 100 m AGL at 1451 UTC (Fig. 4), in association with damaging winds of over 50 m s^{-1} near the surface (not shown). In contrast, MVb and MVc were nondamaging and too weak to be identified as a "significant MV"[1] in XXW15. MVb experienced a lifetime of about 1 h, with

[1] There appears no universal definition in the literature for MVs based upon its intensity, scale, and lifetime, etc. For example, mesovortex was defined of a maximum vertical vorticity > 0.01 s^{-1} in Wheatley and Trapp (2008), while Atkins and St. Laurent (2009a) used a threshold of 0.0125 s^{-1}. As in XXW15, "significant MV" was defined by a peak vertical vorticity > 0.035 s^{-1}. This relatively high threshold is to distinguish intense MVs from many other weak MVs produced in the model.

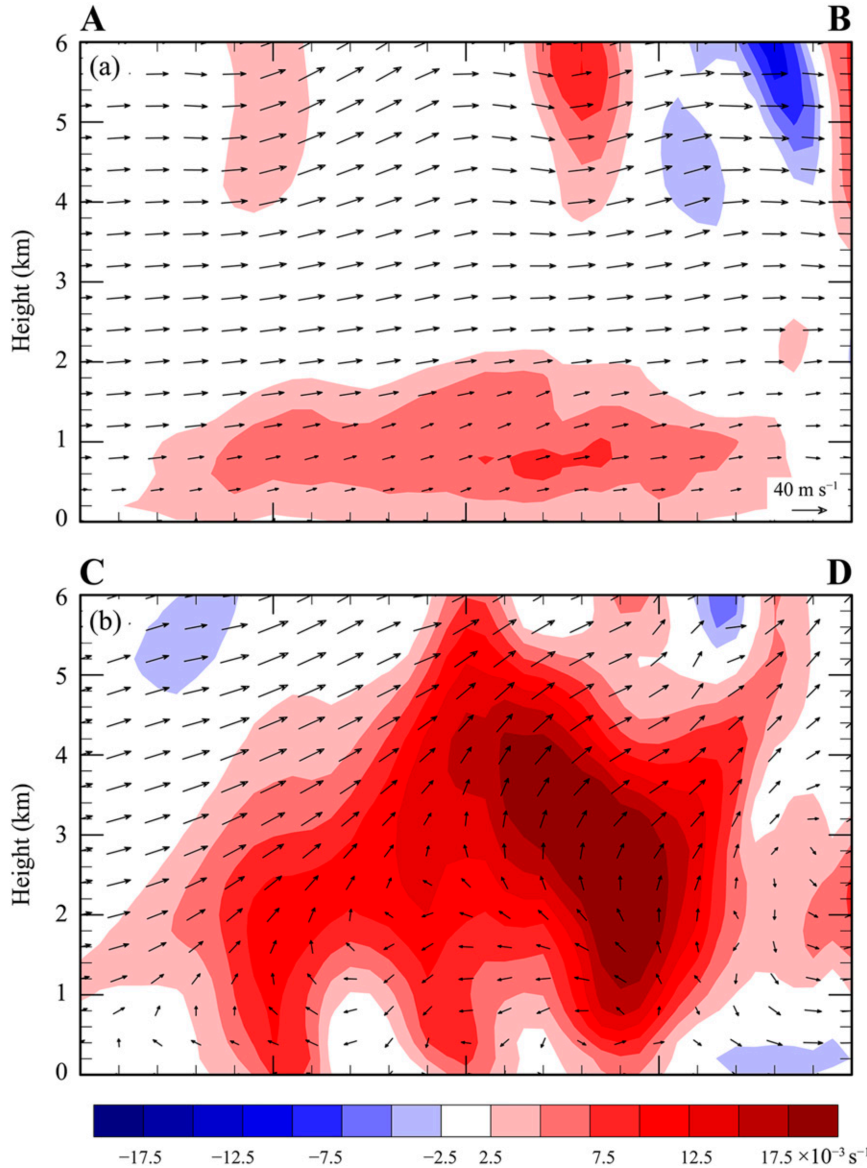

FIG. 3. Vertical planes of vertical vorticity (shading) and storm-relative wind (vectors) at (a) 1415 UTC and (b) 1425 UTC. Positions of the vertical planes are indicated in Fig. 2. Horizontal tick marks are spaced 1.6 km apart (i.e., two horizontal grids).

a peak vertical vorticity of $0.012\,s^{-1}$ (Fig. 4). MVc showed the lowest intensity ($<0.01\,s^{-1}$) and shortest lifetime (<30 min) among the three vortices so its evolution will not be discussed further.

The initial development of MVb preceded that of MVa. It reached a vertical vorticity of $0.01\,s^{-1}$ at 100 m AGL by 1428 UTC, 7 min earlier than MVa (Fig. 4). After that, MVb moved away from MVa (and away from the bow echo apex), exhibiting no appreciable upscale growth (Fig. 5). The maximum vorticity of MVb fluctuated around $0.01\,s^{-1}$, with two more peaks developed at 1445 and 1502 UTC (Fig. 4). It finally decayed at about 1515 UTC (not shown).

The evolution of MVa differed significantly from that of MVb. It stayed near the bow apex all the time and first developed a moderate vertical vorticity of $0.018\,s^{-1}$ at 1438 UTC (Fig. 4). During this time, the downdrafts north of MVa intensified and produced a northerly outflow that caused its elongated axis to rotate cyclonically with time (Figs. 5b,c). Meanwhile, a secondary vortex center developed west of the original MVa vortex center, leading to a two-vortex-center structure (Fig. 5c). Over the next few minutes, the downdrafts north of MVa strengthened again and divided MVa into two parts. The western part moved westward and dissipated rapidly (Fig. 5d) while the eastern

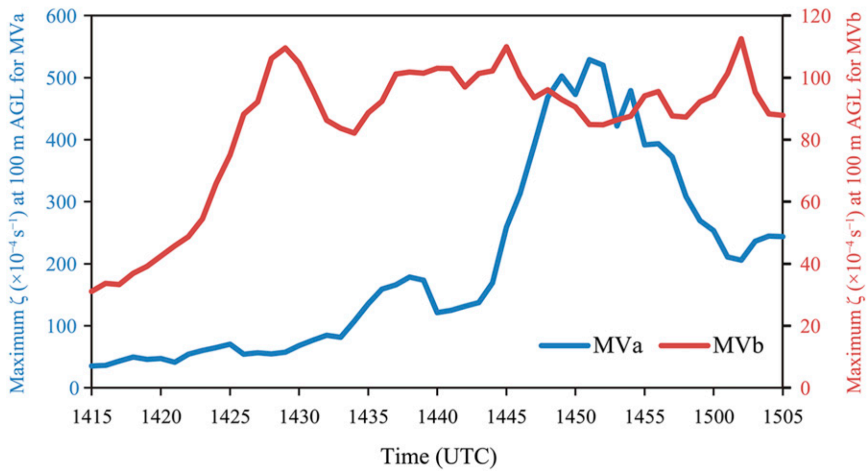

FIG. 4. Time sequences of the maximum vertical vorticity (ζ) for MVa and MVb at 100 m AGL from 1415 to 1505 UTC.

part of MVa grew into a more intense mesovortex at 1448 UTC (Fig. 5e) with a vertical vorticity of $0.47\,s^{-1}$. The strong rotation of MVa maintained for about 6 min and reached its peak intensity of $0.053\,s^{-1}$ at 1451 UTC (Fig. 4). It then weakened with time, accompanied by intrusion of downdrafts into the vortex center (Fig. 5f). As studied by Trapp and Weisman (2003), these downdrafts were driven by the downward-directed pressure gradient force that was dynamically induced by the intense low-level rotation. The later evolution of MVa will not be discussed further since its vertical vorticity remained below $0.05\,s^{-1}$ (see XXW15).

c. Downdrafts and MV development

As discussed earlier, notable downdrafts developed behind MVa at 1445 UTC (Fig. 5d), prior to its rapid intensification to become a strong mesovortex. Growth of MVb from 1425 to 1430 UTC was also preceded by the development of downdrafts on its rear flank (northwest side in this case; not shown). Downdrafts behind MVb were localized, underneath the sloping, rearward-tilted updrafts, with maximum downward speed of $<10\,m\,s^{-1}$ at about 2.6 km AGL (Fig. 6a). In contrast, MVa was embedded within strong rear inflows behind the bow apex that were part of a broad system-scale RIJ. The descending RIJ was characterized by strong subsidence in excess of $15\,m\,s^{-1}$ at 1.8 km AGL behind MVa (Fig. 6b); it also promoted stronger and deeper low-level lifting through stronger horizontal convergence on the forward flank (east–northeast side) of MVa as compared to the MVb case.

Strong downdrafts behind the MVs work to enhance the low-level convergence and thus the vertical stretching of vorticity on the MV forward flank (Figs. 7a,c). Additionally, the downdraft, in conjunction with forward-flank updraft, also acts to tilt the vortex line efficiently such that the tilting generation of vertical vorticity is comparable to vertical stretching (Figs. 7b,d). The tilting pattern is indicative of strong uplifting of vortex lines for MVb (Fig. 7b), whereas the downward tilting by the downdraft is as strong for MVa (Fig. 7d). For both cases, the maximum titling generation of vorticity consistently occurs at the boundary of downdraft and updraft. While MVb remains weak, MVa eventually develops into an intense mesovortex because it experiences much stronger stretching and tilting as promoted by the strong downdraft core that is connected with the descending RIJ of the system at the bow apex; the cause of the intensifying RIJ was discussed in XXW15 as being dynamically forced.

The above analyses reveal the importance of downdrafts in producing the near-surface vertical rotation, which had been well recognized (Davies-Jones 1982a,b; Walko 1993; Markowski 2002). In general, downward tilting of horizontal vorticity was considered to be more effective than upward tilting in producing large vertical vorticity next to the ground because air parcels in the latter case would rise away from the surface and only acquire a notable vertical vorticity aloft. Moreover, the surging outflow of downdrafts can help enhance the low-level convergence and hence the vertical stretching of vertical vorticity. Enhancement of convergence by rear-flank downdrafts or internal cold-pool air surges within tornadic supercells has been documented by radar observational studies (e.g., Lemon and Doswell 1979; Marquis et al. 2008; Lee et al. 2012). Tornadogenesis and tornado maintenance have also been found in close relationship with intensifying downdrafts (Marquis et al. 2012; Kosiba et al. 2013).

Moreover, it is interesting to note that the near-surface horizontal vorticity is generally crosswise, pointing toward north–northeast (to the left of velocity vectors) near

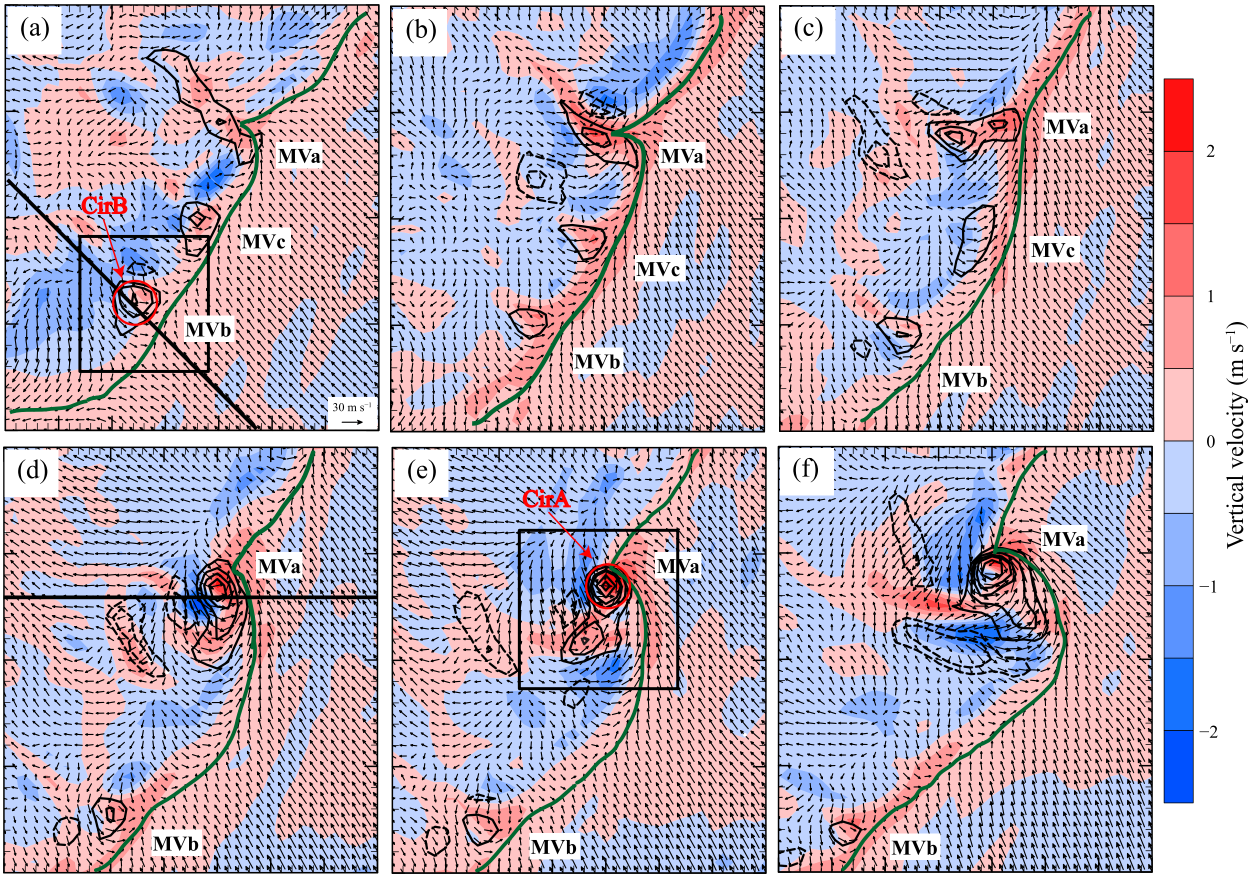

FIG. 5. Evolution of MVa and MVb at (a) 1428 UTC, (b) 1435 UTC, (c) 1440 UTC, (d) 1445 UTC, (e) 1448 UTC, and (f) 1455 UTC. The storm-relative wind (vectors), vertical velocity (shading), and vertical vorticity (contours) at 100 m AGL are shown. Negative vertical vorticity of $(-5, -2.5) \times 10^{-3}\,\mathrm{s}^{-1}$ are contoured in dashed lines. Intervals of positive vertical vorticity are $(2.5, 5, 10) \times 10^{-3}\,\mathrm{s}^{-1}$ in (a) and $(5, 10, 15, 20, 30, 40) \times 10^{-3}\,\mathrm{s}^{-1}$ in all others. Green lines represent the gust front position and are drawn manually. In (a) and (d), black straight lines indicate the positions of vertical planes shown in Fig. 6. In (a) and (e), black boxes denote the domains shown in Figs. 7 and 8, and red circles indicate the material circuits CirB and CirA under examination. Tick marks are spaced 0.8 km apart.

the mesovortex in our case (Fig. 8). Given the buoyancy field[2] as represented by the perturbed virtual potential temperature in Fig. 8, the low-level horizontal vorticity is in the opposite direction as would be generated baroclinically near the gust front. Large horizontal vorticity exceeding $0.1\,\mathrm{s}^{-1}$ is found near the ground, underneath a local wind speed maxima (Fig. 9). At higher levels the horizontal vorticity became much weaker, orientated in a direction more consistent with baroclinic generation. The high horizontal vorticity within the surface-based layer must have been generated by surface friction, which will be addressed next.

[2] As noted in Markowski et al. (2002) and Shabbott and Markowski (2006), buoyancy is proportional to the perturbation of virtual potential temperature θ_v (when liquid water is included in its definition). In the text, for simplicity, the θ_v field subtracting 300 K is used to denote the buoyancy field. The direction of baroclinically generated horizontal vorticity can be inferred from the θ_v field.

4. Equations of circulation and vorticity

a. Circulation equation

Because the MVs are generated near the surface, the Boussinesq approximation is applicable (Adlerman et al. 1999). With this assumption, the Bjerknes' circulation theorem for nonrotating atmosphere can be written as

$$\frac{DC}{Dt} = \oint (b\mathbf{k} + \mathbf{F}) \cdot d\mathbf{l}, \tag{1}$$

where $C = \mathbf{V} \cdot d\mathbf{l}$ is the circulation, $\mathbf{V} = (u, v, w)$ is the velocity, $d\mathbf{l}$ is an element of the material circuit along which the integration is performed (in counterclockwise direction), b is the buoyancy, $\mathbf{k}$ is the unit vector in the

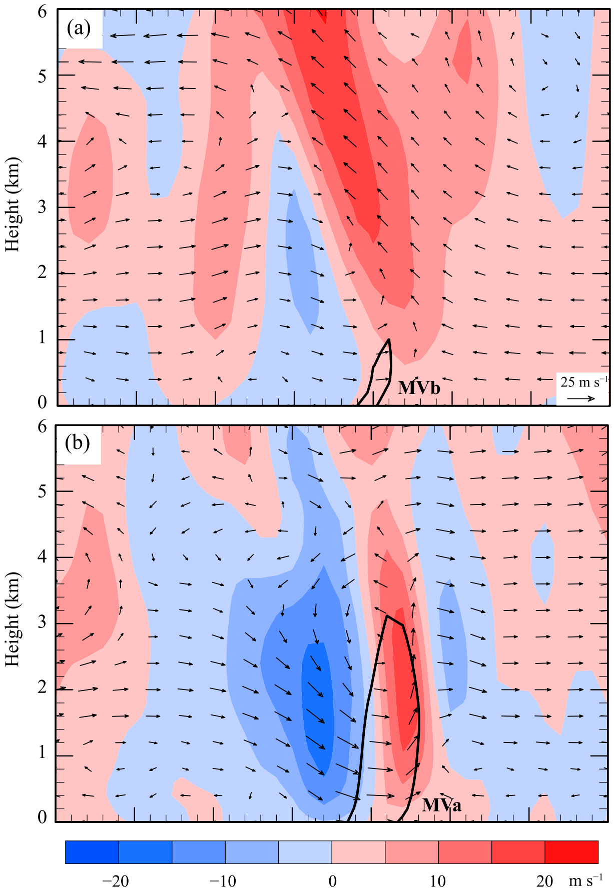

FIG. 6. Vertical velocity in the vertical plane through (a) MVb at 1428 UTC and (b) MVa at 1445 UTC. Arrows denote the storm-relative winds; black contour lines represent the $0.01\,\mathrm{s}^{-1}$ vertical vorticity. Positions of the vertical planes are indicated by black straight lines in Figs. 5a,d. Horizontal tick marks are spaced 0.8 km apart.

vertical z direction, and $\mathbf{F} = (F_x, F_y, F_z)$ is made up of the turbulent mixing terms in the momentum equations, which is dominated near the ground by the vertical momentum flux divergence. At the ground level, the momentum flux is defined by the surface drag that is always in the opposite direction as the flow; in other words, the momentum flux at the surface is always downward, causing deceleration of flow at the surface. For simplicity, we refer to $\mathbf{F}$ as the frictional force including surface friction and subgrid-scale turbulence mixing. The buoyancy force b is given by

$$b = g\left(\frac{\theta'}{\overline{\theta}} + 0.61q_v' - q_w\right), \tag{2}$$

where g is the gravitational acceleration, θ' and q_v' are the perturbations of potential temperature (θ) from a certain reference state and water vapor mixing ratio (q_v), and q_w is the sum of liquid and solid hydrometeor mixing ratios. The reference state quantities [e.g., $\overline{\theta}(z)$ and $\overline{q}_v(z)$] are derived from the inflow air as suggested by Grzych et al. (2007). The model output θ and q_v at 1-min interval are first averaged over an area of $24 \times 24\,\mathrm{km}^2$ ahead of the bow apex. Then the area-mean potential temperature and water mixing ratio are averaged again over a time interval (Δt) to obtain the time-independent reference states. The length of Δt depends on the period over which the Lagrangian circulation analysis is performed.

According to Stokes's theorem, the circulation Eq. (1) can be rewritten as

$$\frac{DC}{Dt} = \oiint (\nabla \times b\mathbf{k} + \nabla \times \mathbf{F}) \cdot d\mathbf{A}, \tag{3}$$

where $\mathbf{A}$ is the surface bounded by the circuit and $\nabla \times b\mathbf{k}$ and $\nabla \times \mathbf{F}$ are separately the baroclinic and frictional generation of vorticity. As shown in (4)–(6) below, baroclinicity can only produce horizontal vorticity, while friction is able to create all three components of vorticity. However, generation of vertical vorticity by friction is usually very small compared to the generation of horizontal vorticity by friction near ground. In this regard, circulation about a circuit is considered to change as the baroclinically and frictionally generated horizontal vortex lines pass through the vertical projection of the circuit (e.g., Atkins and St. Laurent 2009b).

b. Vorticity equation

The equation governing the vertical vorticity (ζ) is

$$\frac{D\zeta}{Dt} = \boldsymbol{\omega}_h \cdot \nabla_h w + \zeta\frac{\partial w}{\partial z} + \left(\frac{\partial F_y}{\partial x} - \frac{\partial F_x}{\partial y}\right), \tag{4}$$

where $\boldsymbol{\omega}_h$ is the horizontal vorticity. Physically, the first term on the right-hand side (rhs) of (4) denotes the reorientation of horizontal vorticity into vertical via tilting; the second term represents the stretching of vertical vorticity; the last term designates the frictional generation of vertical vorticity due to horizontal gradient of the frictional force.

For convenience, the horizontal vorticity is decomposed into streamwise (ω_s) and crosswise (ω_n) components in the semi-natural coordinates ($\mathbf{s}, \mathbf{n}, \mathbf{k}$), where $\mathbf{s}$ is along the horizontal wind (V_H) direction and $\mathbf{n}$ is directed perpendicularly to the left of $\mathbf{s}$ (Lilly 1982; Adlerman et al. 1999). The equations that control ω_s and ω_n are given as follows (Mashiko et al. 2009; Schenkman et al. 2014):

$$\frac{D\omega_s}{Dt} = \omega_n\frac{D\psi}{Dt} - \left(\frac{\partial w}{\partial s}\frac{\partial V_H}{\partial n} - V_H\frac{\partial \psi}{\partial s}\frac{\partial V_H}{\partial z}\right) + \omega_s\frac{\partial V_H}{\partial s} + \frac{\partial b}{\partial n} + \left(\frac{\partial F_z}{\partial n} - \frac{\partial F_n}{\partial z}\right) \quad \text{and} \tag{5}$$

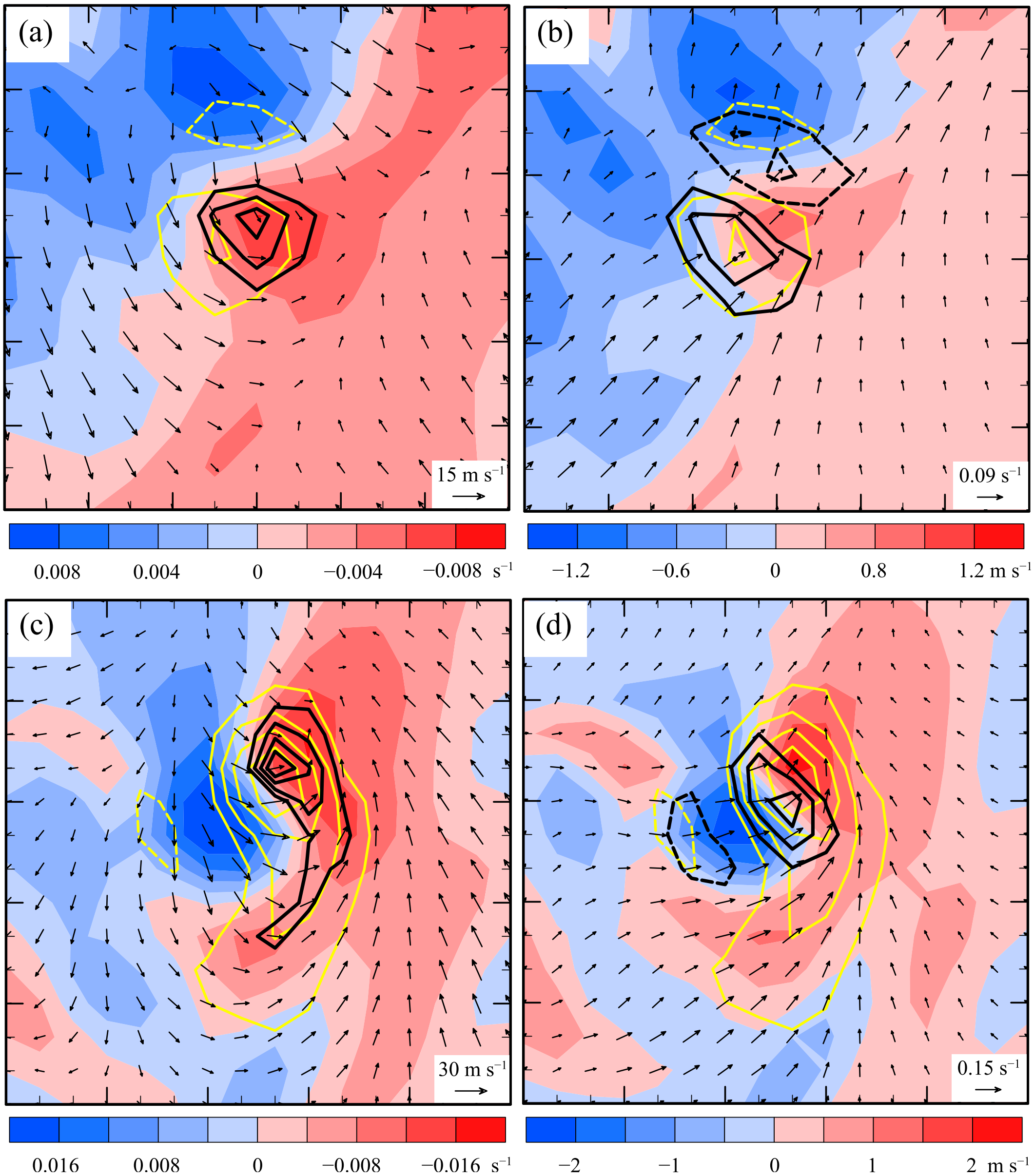

FIG. 7. (a),(c) Horizontal wind convergence (shading) and vertical stretching generation of vertical vorticity (black contours) and (b),(d) vertical velocity (shading) and tilting generation of vertical vorticity (black contours) at 100 m AGL. Here (a) and (b) are for MVb at 1428 UTC, while (c) and (d) are for MVa at 1445 UTC, with the plotted domains indicated in Figs. 5a and 5d. Vectors denote storm-relative winds in (a) and (c) and horizontal vorticity in (b) and (d). Yellow contours represent the vertical vorticity values of $(-2.5, 5.0, 10) \times 10^{-3}\,\mathrm{s}^{-1}$ in (a) and (b) and $(-5, 5, 10, 15, 20) \times 10^{-3}\,\mathrm{s}^{-1}$ in (c) and (d). Tick marks are spaced 0.8 km apart.

$$\frac{D\omega_n}{Dt} = -\omega_s\frac{D\psi}{Dt} - \left(V_H\frac{\partial V_H}{\partial n}\frac{\partial \psi}{\partial z} - V_H\frac{\partial w}{\partial n}\frac{\partial \psi}{\partial s}\right) + \omega_n V_H\frac{\partial \psi}{\partial n} - \frac{\partial b}{\partial s} + \left(\frac{\partial F_s}{\partial z} - \frac{\partial F_z}{\partial s}\right), \qquad (6)$$

where $\psi = \tan^{-1}(v/u)$ is the azimuth of V_H. The first term on the rhs of the above equations represents the exchange between ω_s and ω_n as the horizontal wind changes its direction ψ. This term is notable near an intense vortex where the flow is strongly curved. The other terms denote the tendencies of ω_s and ω_n caused by tilting, stretching, baroclinicity, and friction, respectively.

c. *Analysis methodology*

For a given material circuit, the model winds at 20-s interval are used to compute the trajectories of air parcels on this circuit. The calculation is performed using

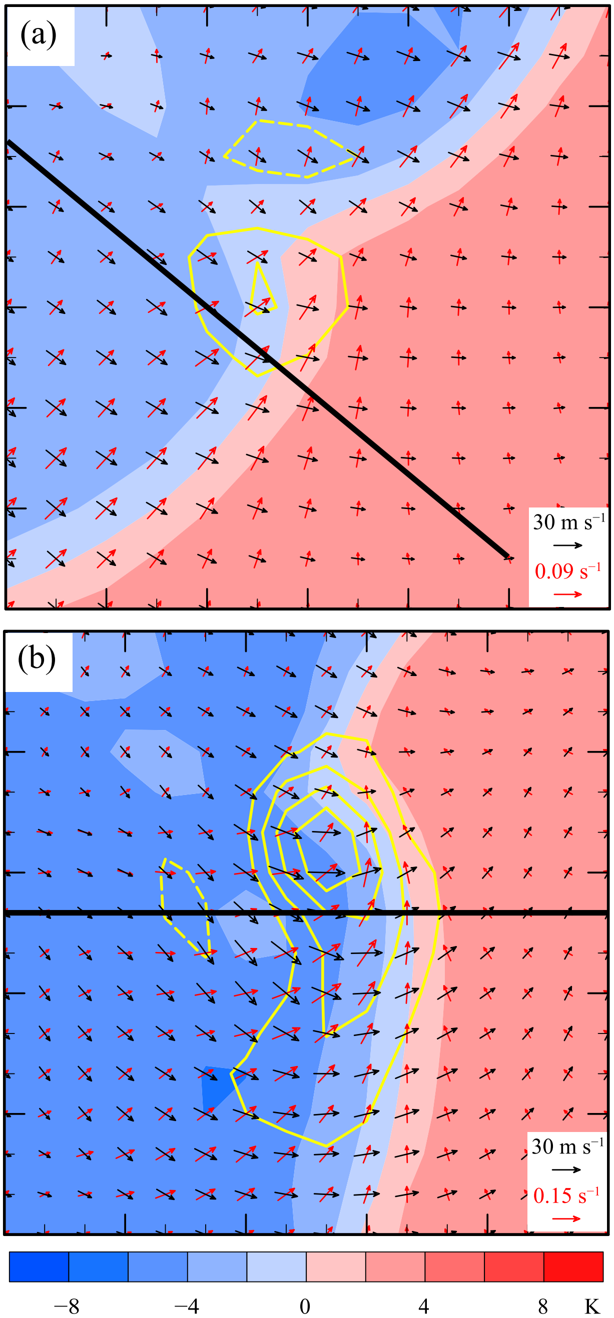

FIG. 8. Ground-relative wind (black vectors), horizontal vorticity (red vectors), and virtual potential temperature (shading) at 100 m AGL for (a) MVb at 1428 UTC and (b) MVa at 1445 UTC. The plotted domains are indicated in Figs. 5a and 5d. Yellow contours denote vertical vorticity at intervals of $(-2.5, 5.0, 10) \times 10^{-3}\,\mathrm{s}^{-1}$ in (a) and $(-5, 5, 10, 15, 20) \times 10^{-3}\,\mathrm{s}^{-1}$ in (b). Black straight lines indicate the positions of vertical planes shown in Fig. 9. Tick marks are spaced 0.8 km apart.

a trajectory program within the ARPS model system, called ARPSTRAJC, which uses the second-order trapezoidal scheme with iterations for time integration. To use this program for the WRF simulation, a well-tested program called wrf2arps is used to convert the WRF gridded fields to the ARPS gridded fields. The circulation of the circuit can be calculated from the wind vectors interpolated to the trajectory points made up of the circuit. Note that the winds at the first model level above ground are used whenever the parcel drops below this level. The buoyancy term is interpolated from the model grid to the circuit trajectory points. However, the frictional term is not calculated directly; instead, it is diagnosed as the residual of the circulation tendency and the buoyancy term. This choice is dictated by the fact that the turbulent momentum exchange coefficient required to recalculate the turbulent mixing terms is not a diagnostic variable within the MYJ PBL scheme in the present WRF model simulation and would require significant efforts writing it out. This indirect estimate, while not ideal, can be reasonably justified. For one thing, the circulation equation is very simple, containing only two source terms (i.e., baroclinicity and friction). For another, calculations of circulation and baroclinicity involve only line integrals with appreciable accuracy. Vorticity budgets are handled in a similar manner [i.e., the frictional terms in (4)−(6) are indirectly diagnosed]. This may be less justifiable than the circulation analysis, because the vorticity equations, especially those of horizontal vorticity, consist of more source terms. Furthermore, each forcing term involves spatial derivatives which are more prone to error compared to line integrals. Still, based on our analyses that appear to be physically consistent, we believe our results are at least qualitatively correct.

5. Lagrangian circulation analysis

a. *Analysis of MVb: 1416–1428 UTC*

The circulation about a circular material circuit (CirB) that encloses MVb at 100 m AGL, or at the "foot" of MVb, at 1428 UTC, and its earlier states through backward trajectory calculations (see Fig. 5a), are first examined. The circuit at 1428 UTC has a radius of 1.5 km, with parcels sampled every 0.1° along the circuit. The parcels on CirB are integrated backward 12 min to 1416 UTC. This relatively short backward time tracking is because CirB becomes contorted quickly as one integrates backward in time, thus hindering meaningful circulation analysis if traced back further.

As shown in Figs. 10a,b, the southeastern portion of CirB stays close to the ground and originates from the warm sector ahead of the gust front. In contrast, the northwestern part of the circuit slopes upward and originates from the rear of the gust front, with the northwesternmost portion positioned at ~(500–700) m AGL 12 min earlier. Over time, the rear-flank circuit descends markedly whereas the prefrontal circuit undergoes a gentle ascent. Finally, the entire circuit converges at the gust front, shrinking to the small circular circuit at 1428 UTC (Fig. 10a)—the time

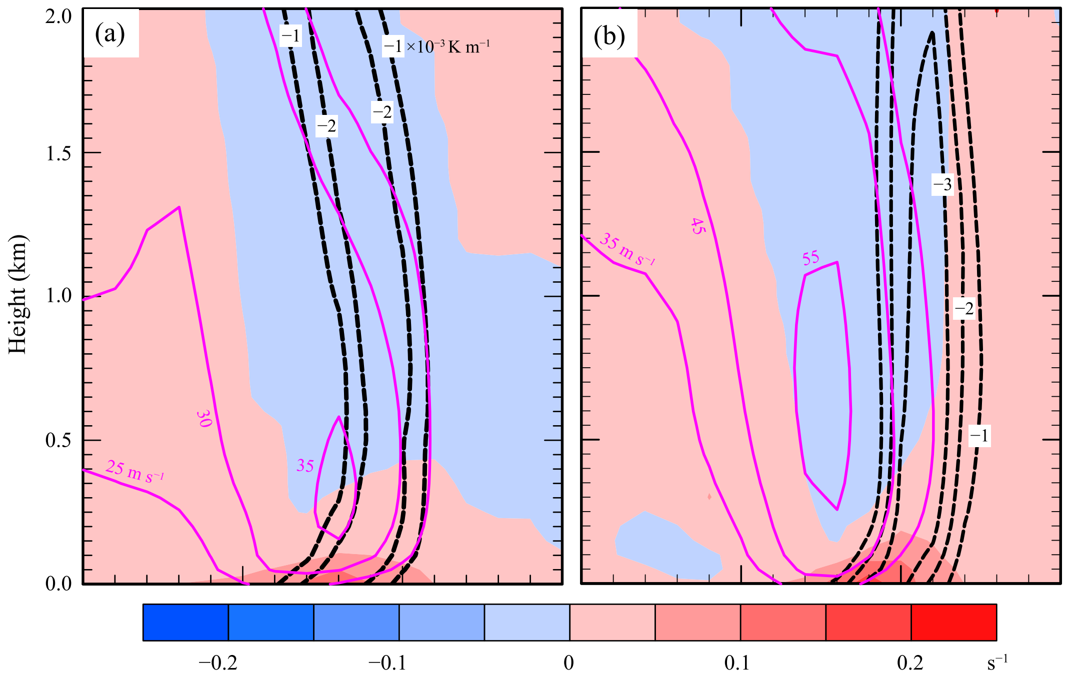

FIG. 9. Horizontal vorticity (shading) and baroclinic generation of horizontal vorticity (represented by horizontal gradient of virtual potential temperature; black contour lines) normal to the vertical planes through (a) MVb at 1428 UTC and (b) MVa at 1445 UTC. Ground-relative wind speed (magenta contours) is also shown. Positions of the vertical planes are indicated by black straight lines in Fig. 8. Horizontal tick marks are spaced 0.8 km apart.

when this circuit was initialized. The circulation of CirB increases from $3.8 \times 10^4\,m^2\,s^{-1}$ at 1416 UTC to $4.8 \times 10^4\,m^2\,s^{-1}$ at 1427 UTC, followed by a slight decrease at 1428 UTC (Fig. 10c). Before 1423 UTC, the increase of circulation is mainly accounted for by baroclinic generation and much of this generation is canceled out by negative generation by the friction. After 1423 UTC, however, the frictional generation becomes dominantly positive (Fig. 10d), causing the repaid increase of the circulation before 1427 UTC (Fig. 10c). The negative circulation generation by friction in the final couple of minutes before 1428 UTC should be because of the slowing down by surface drag acting on the circuit as the circuit becomes horizontal and is close to the ground.

At 1420 UTC, the northern part of CirB is positioned at a high altitude. The normal vector (positive in the direction of mean vorticity associated with the circuit) of the material surface bounded by the B–E segment is predominantly southward (Fig. 11a). Seen from the buoyancy field, baroclinicity produces a large amount of southward component of horizontal vorticity that passes through the tilted surface bounded by B–E (Fig. 12a).[3] According to (3), a positive circulation tendency of $37\,m^2\,s^{-2}$ is thus produced by baroclinicity (Fig. 10d). Conversely, friction causes a negative circulation tendency of $-21\,m^2\,s^{-2}$ at this time. This occurs as the frictional horizontal vorticity[4] have a notable northward component at the foot of B–E (Fig. 12b). Unlike baroclinicity, the frictional effects are mainly confined to the lowest 200 m above ground, with little contribution aloft. By 1425 UTC, the material circuit CirB has descended significantly, in association with a cyclonic rotation with respect to the vortex center (Fig. 11b). At this time the material surface bounded by A–G is vertically tilted, with the normal vector of its vertical projection mainly oriented toward east (i.e., perpendicular to the baroclinically generated horizontal vorticity). Baroclinicity induces a positive circulation tendency in A–C, which is, however, largely cancelled by its negative contributions along E–G (Fig. 12c). In consequence, the baroclinic generation of circulation decreases sharply (Fig. 10d). Meanwhile, as the tilted surface is rotated to the west–southwest of the mesovortex where northerlies and northwesterlies are present, eastward/northeastward

[3] Indeed, at different heights, baroclinic vorticity vector pierces the tilted surface at different positions rather than at a single plane. Nonetheless, baroclinic vorticity are of fairly small variations near the tilted surface.

[4] Frictional horizontal vorticity is estimated from the horizontal wind, assuming that friction near the surface is of the form $\mathbf{F} = (C_d|\mathbf{V}_h|\mathbf{V}_h)/\Delta z$, where C_d is the drag coefficient and $\mathbf{V}_h$ is the horizontal velocity and Δz is the near-surface layer depth over which the vertical momentum flux becomes negligible.

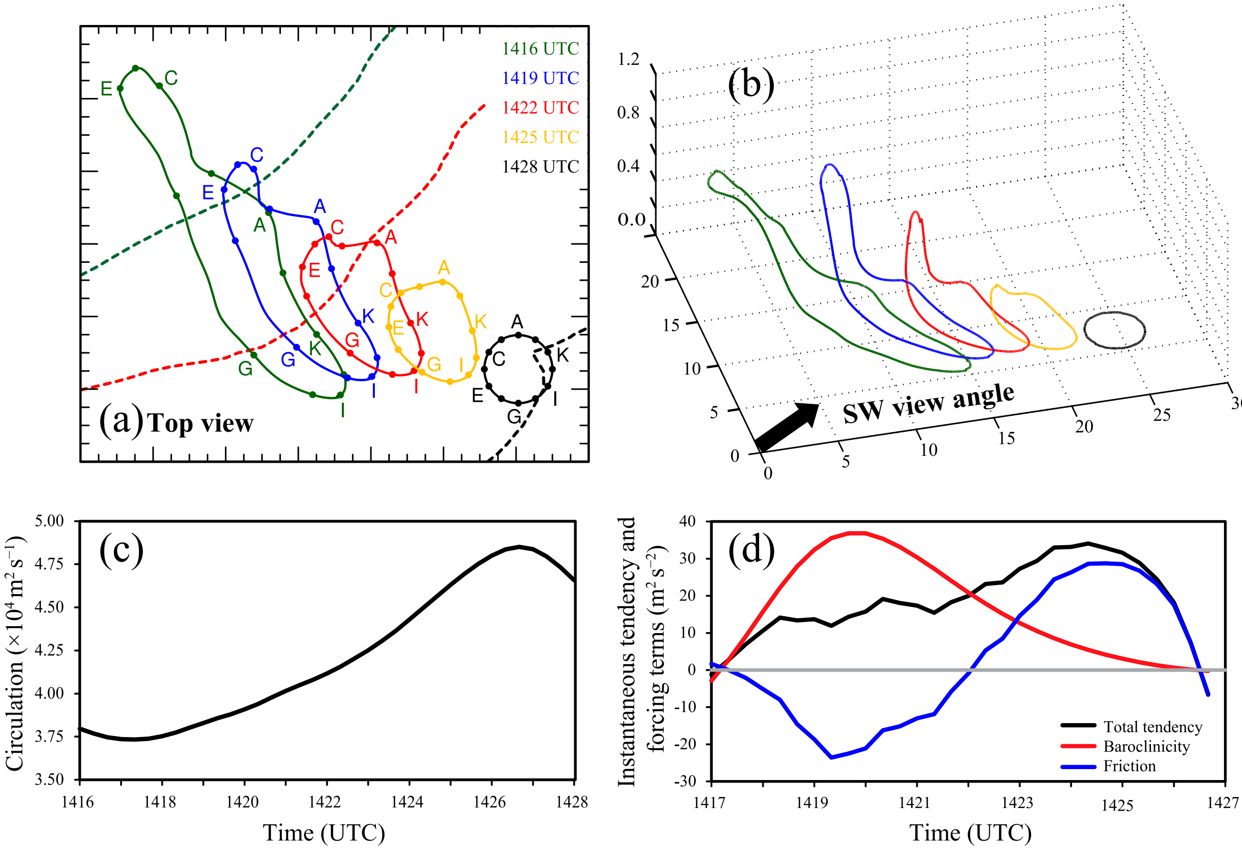

FIG. 10. (a) Top view of the ground-relative track of material circuit CirB in the period 1416–1428 UTC. Dashed lines mark the locations of squall-line gust front at (left to right) 1416, 1422, and 1428 UTC. (b) As in (a), except for the three-dimensional perspective viewed from southwest. (c) Time sequence of the circulation about CirB during 1416–1428 UTC. (d) As in (c), but for instantaneous circulation tendency and its corresponding forcing terms, with three-point moving average applied to filter the intra-minute fluctuations. Tick marks in (a) are spaced 0.8 km apart.

horizontal vorticity are created by friction at the low levels (Fig. 12d). The frictional horizontal vorticity produces a positive circulation tendency of $29\,\mathrm{m^2\,s^{-2}}$ when the vorticity vectors pass through the tilted surface associated with the circuit. These analyses demonstrate the import contributions of surface friction to vorticity generation in the air parcels as they feed MVb at the final stage.

b. Analysis of MVa: 1436–1448 UTC

A similar material circuit CirA encircling MVa at 100 m AGL at 1448 UTC (see Fig. 5e) is tracked backward 12 min to 1436 UTC, at which time the structure of CirA has already become somewhat complicated (Figs. 13a,b). The parcels making up CirA also originate from both ahead of and behind the gust front. The eastern portion of CirA is located next to the ground and ascends with time, whereas its western and northern portions experience descent from up to 2 km level (Fig. 13b). On reaching its final position at the gust front, the area of CirA shrinks significantly as well. Unlike CirB, the circulation of CirA first decreases from a high value of $1.68 \times 10^5\,\mathrm{m^2\,s^{-1}}$ at 1436 UTC to $1.43 \times 10^5\,\mathrm{m^2\,s^{-1}}$ at 1442 UTC; it then increases steadily to $1.71 \times 10^5\,\mathrm{m^2\,s^{-1}}$ at 1447 UTC and finally drops slightly near 1448 UTC (Fig. 13c). As shown in Fig. 13d, changes of circulation are mainly caused by friction while baroclinicity only plays a secondary role.

At 1438 UTC (Fig. 14a), the material surfaces bounded by segments B1–G1 and G2–G4 are vertically tilted toward northwest and northeast respectively. (Point B1 is within the segment B–C, while points G1 to G5 are within G–H. These points are drawn to ease description.) For both tilted surfaces, their vertical projections are in general parallel to the nearby gust front, hence giving rise to rather weak baroclinic circulation tendency (Fig. 13d). In contrast, friction creates a large, negative tendency of $-100\,\mathrm{m^2\,s^{-2}}$, since the frictional horizontal vorticity have prominent northwestward component at the foot of B1–G1 (Fig. 15a). Friction also appears to contribute negatively to the circulation along G2–G4, yet it is expected to be

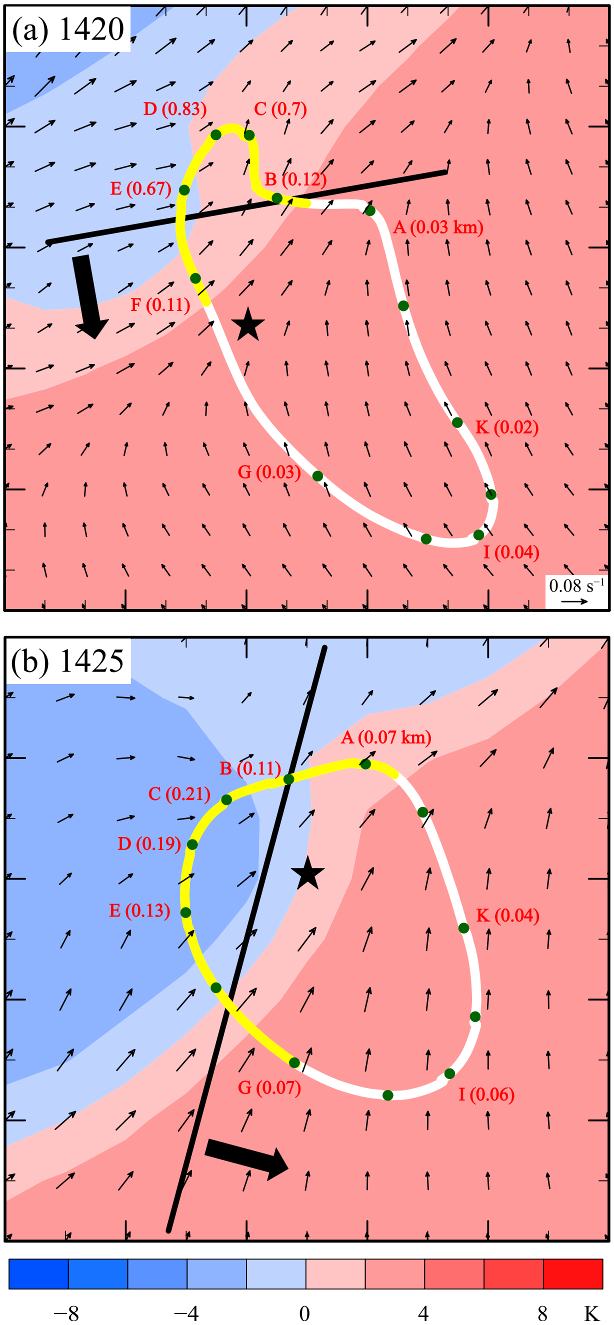

FIG. 11. Material circuit CirB at (a) 1420 UTC and (b) 1425 UTC. Heights of selected parcels on the circuit are given in the parentheses. Also shown are the virtual potential temperature (shading) and horizontal vorticity (vectors) at 50 m AGL. Positions of the vertical planes shown in Fig. 12 are denoted by black straight lines with their positive directions indicated by black thick arrows. Black stars mark the locations of mesovortex center. The yellow section of the circuit corresponds to the yellow section shown in Fig. 12. Tick marks are spaced 0.8 km apart.

weak given the small vertical projection of the material surface bounded by G2–G4. At 1445 UTC, the tilted segment B–G reaches low level below 500 m AGL and rotates from northeast of the vortex center to its northwest/west (Fig. 14b). As in the late stage of MVb, northeastward–eastward horizontal vorticity are frictionally generated at low levels beside C–G and pierce the tilted surface (Fig. 15b), resulting in a positive circulation tendency of 97 $m^2 s^{-2}$ (Fig. 13d). Meanwhile, baroclinicity also contributes positively though by a small amount to the total circulation, because the positive (baroclinic) circulation tendency in B–F dominates the negative one in G–H (not shown).

The above Lagrangian circulation analyses indicate the importance of friction in contributing to the circulation associated with low-level MVs, which had not been documented before in the context of MVs as far as we know. Vorticity budgets for selected air parcels will be shown in the next to further highlight the important role played by friction.

6. Lagrangian vorticity budget analysis

As noticed in section 4c, vorticity analysis tends to be less accurate than that of circulation, since vorticity equations contain more source terms which involve derivatives of velocity. Thus, if the frictional term is diagnosed as the residual of total vorticity tendency and all other source terms, it may be contaminated by numerical errors of finite differencing. To find ''reliable'' vorticity budgets, the following two assumptions are considered: (i) friction is unimportant for direct vertical vorticity generation but important for horizontal vorticity; that is, the frictional term is omitted in (4) but retained in (5) and (6); (ii) if the vertical vorticity budget along a parcel trajectory is accurate, then the budgets of horizontal vorticity along this trajectory are also accurate. In other words, vorticity budgets are considered reliable when the integrated vertical vorticity from (4) (i.e., Lagrangian vertical vorticity) matches well with the Eulerian vertical vorticity interpolated to the parcel's trajectory.

By performing vorticity budgets for all parcels on the two material circuits CirA and CirB, three representative parcels, P1, P2, and P3 (see Fig. 16), are picked to help elucidate the vorticity evolution. P1 and P2 represent rear-inflow parcels descending from aloft, while P3 is a prefrontal-inflow parcel from the low level.

a. Rear-inflow air parcel

Figure 17 shows the vorticity budgets for the rear-inflow parcel P1 on CirB, which first ascends from 330 m AGL to 550 m AGL at 1418 UTC, followed by steady descent to 100 m AGL at 1428 UTC (Fig. 17a). Its

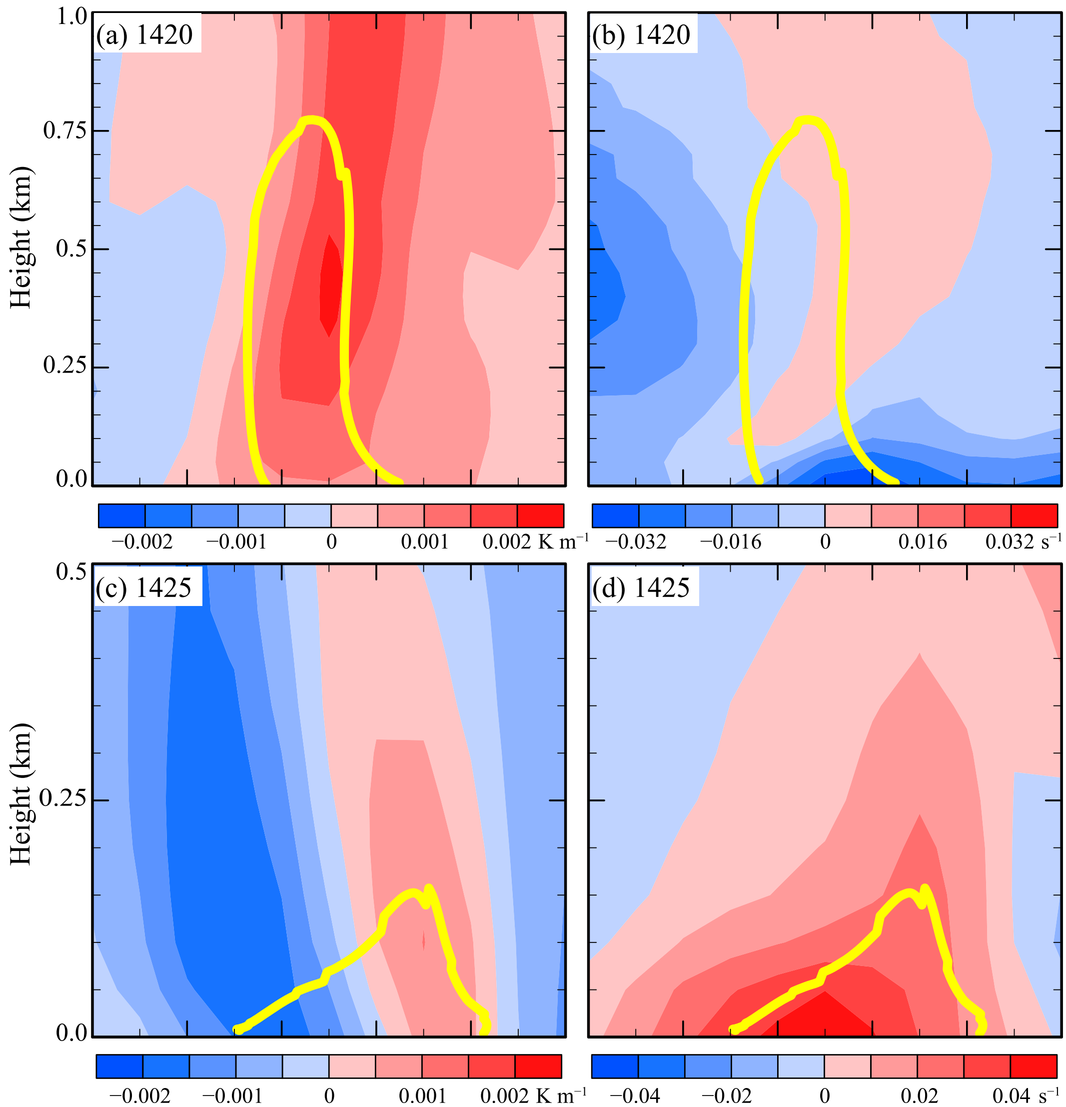

FIG. 12. Baroclinic generation of horizontal vorticity (represented by horizontal gradient of virtual potential temperature) perpendicular to the vertical planes through northwestern CirB at (a) 1420 UTC and (c) 1425 UTC. (b),(d) As in (a) and (c), but for frictionally generated horizontal vorticity (estimated from the horizontal wind). Positions of the vertical planes are indicated by black straight lines in Fig. 11. Positive vorticity are toward the directions indicated by black thick arrows in Fig. 11. Yellow lines denote the projections of CirB colored yellow in Fig. 11. Horizontal tick marks are spaced 0.8 km apart.

vertical vorticity increases rapidly before 1421 UTC as a result of horizontal vorticity tilting. Stretching contributes a little during ascent but soon turns to negative as P1 descends, causing a slight decrease of vertical vorticity after 1421 UTC. Without tilting, the vertical vorticity of P1 would become much smaller. The fact that the rear-inflow parcels acquire vertical vorticity via tilting is in agreement with Trapp and Weisman (2003) and Wheatley and Trapp (2008).

The horizontal vorticity of P1 is predominantly crosswise at 1416 UTC (Figs. 17b,c). In the next 2 min, a positive streamwise vorticity develops from the conversion of crosswise vorticity, while tilting and baroclinic terms add to the growth later (Fig. 17b). As P1 descends toward the surface, the frictional term (estimated as the residual of interpolated and integrated horizontal vorticity) becomes increasingly negative, operating to reduce the streamwise vorticity. The increased frictional generation of horizontal vorticity near the surface is reasonable, because horizontal vorticity is readily affected by surface friction and/or turbulent mixing in the PBL. Consistent with Mashiko et al. (2009), it is the stretching term that accounts for the most notable growth of streamwise vorticity. The large

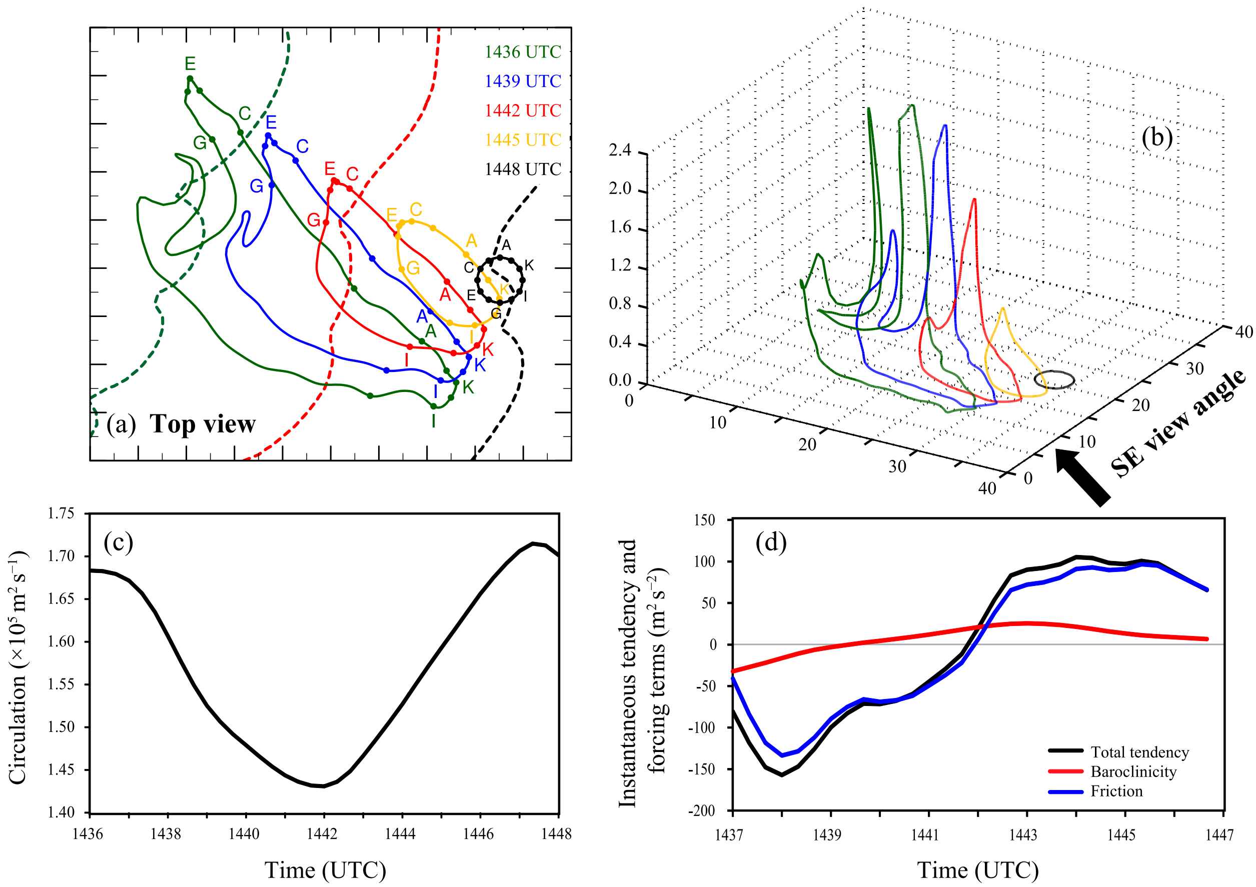

FIG. 13. As in Fig. 10 except for material circuit CirA during 1436–1448 UTC.

stretching generation occurs as expected. As seen from Fig. 16a, localized high winds are produced near the mesovortex because of the superposition of MV vortical flow with the ambient translational flow (Wakimoto et al. 2006b; Atkins and St. Laurent 2009a). Therefore, when approaching MVb from behind (the west side), P1 finds itself in a region with faster winds ahead. In accordance to (5), streamwise vorticity is stretched significantly by the large wind acceleration. For the crosswise vorticity of P1, it first decreases until 1424 UTC, primarily as a result of negative baroclinic and tilting generation (Fig. 17c). As P1 reaches the low level, the crosswise vorticity increases drastically and exceeds the streamwise vorticity again in the last minute. Friction is found responsible for the rapid increase in crosswise vorticity next to the ground, while neither stretching nor exchange term plays an important role.

The selected rear-inflow parcel P2 on CirA descends from a much higher altitude of 1.7 km AGL (Fig. 18a). However, only as it reaches the low level after about 1445 UTC does P2 obtain a large vertical vorticity. Again, the vertical vorticity originates from the reorientation of horizontal vorticity, which augments markedly during this later time (Figs. 18b,c). Like that of P1, the streamwise vorticity of P2 increases as it is greatly stretched near the low-level mesovortex, and the crosswise vorticity is predominantly generated via friction.

b. Prefrontal-inflow air parcel

Vorticity budgets are depicted in Fig. 19 for inflow parcel P3 on CirA, while qualitatively similar results are found for that of inflow parcels on CirB (not shown). P3 remains near the surface until it encounters the gust front around 1444 UTC, before which its vertical vorticity increases slowly via tilting (Fig. 19a). Significant stretching is found when P3 is brought upward at the gust front. Unlike that of rear-inflow parcels, tiling accounts for only a small portion of the total increase of vertical vorticity; nevertheless, it works to provide the initial vertical vorticity (or add to the preexisting vertical vorticity) for subsequent stretching.

The horizontal vorticity of P3 is almost purely crosswise at 1436 UTC, along with negligible streamwise component (Figs. 19b,c). Considering its large value of $0.05\,\mathrm{s}^{-1}$, which is beyond the typical environmentally

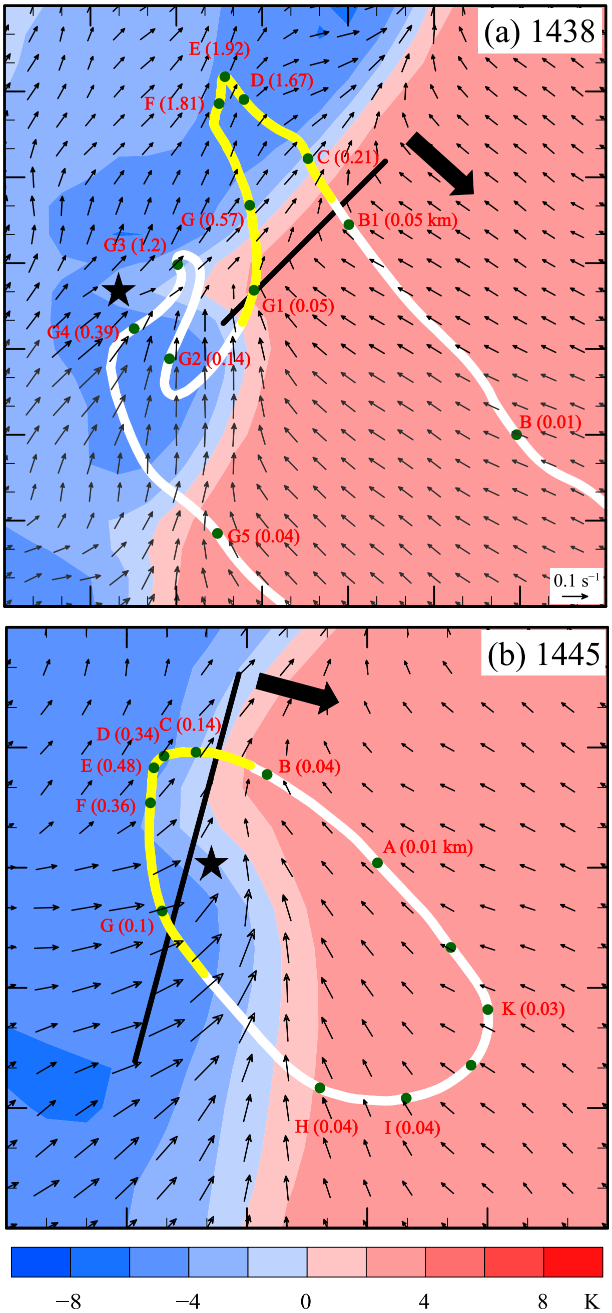

FIG. 14. As in Fig. 11, but for CirA at (a) 1438 UTC and (b) 1445 UTC. Positions of the vertical planes are shown in Fig. 15. The yellow section of the circuit corresponds to the yellow section shown in Fig. 15.

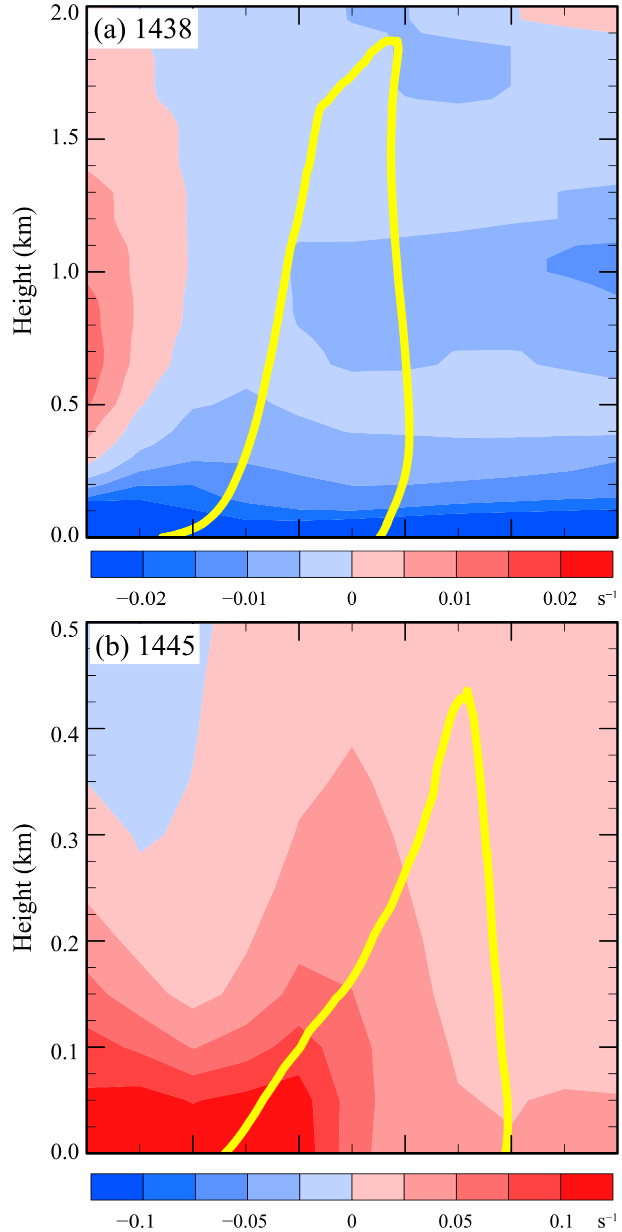

FIG. 15. Frictionally generated horizontal vorticity (estimated from the horizontal wind) perpendicular to the vertical planes through MVa at (a) 1438 UTC and (b) 1445 UTC. Positions of the vertical planes are indicated by black straight lines in Fig. 14. Positive vorticity are toward the directions indicated by black thick arrows in Fig. 14. Yellow lines denote the projections of CirA colored yellow in Fig. 14.

vertical wind shear in the free atmosphere, the crosswise horizontal vorticity is expected to have been created by friction. Both streamwise and crosswise horizontal vorticity components show an increasing trend with time, but only in the last few minutes does the streamwise vorticity become comparable to its crosswise counterpart. Hence, it is basically the crosswise vorticity that is reoriented into vertical for stretching.

Similar to the rear-inflow parcels, friction is also the main contributor to the crosswise vorticity of P3 prior to its rising away from ground (Fig. 19c). However, its streamwise vorticity primarily results from tilting rather than

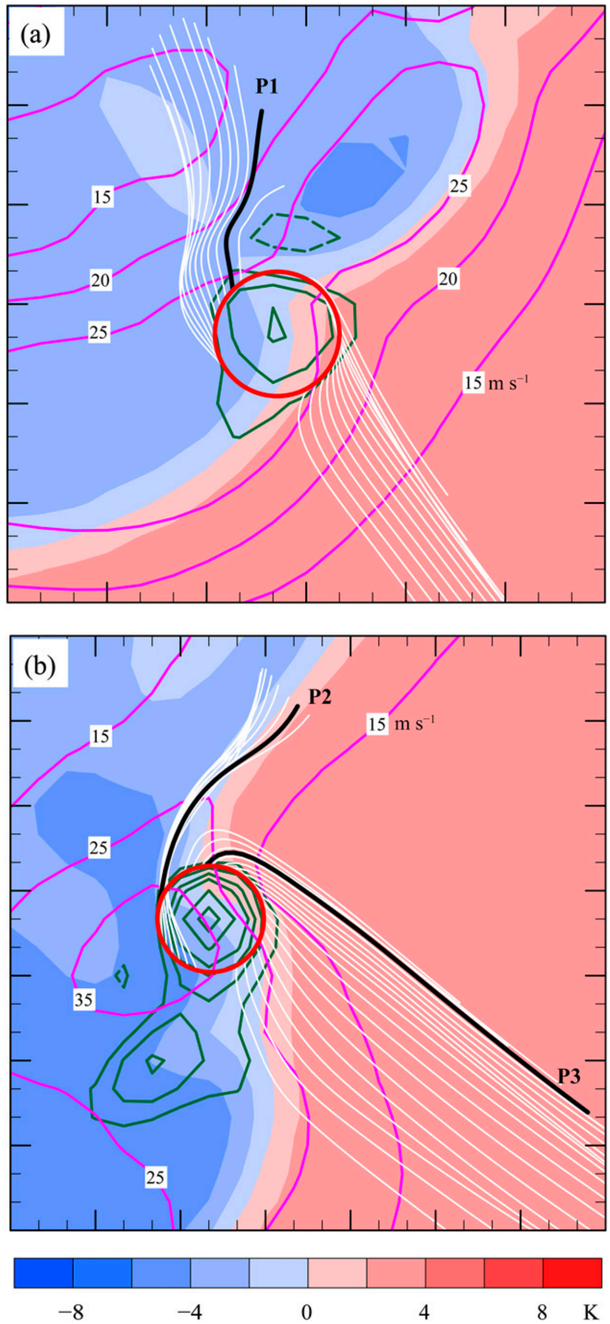

FIG. 16. Vortex-relative trajectories of selected parcels on (a) CirB during 1416–1428 UTC and (b) CirA during 1436–1448 UTC. Circuits' positions at 1428 and 1448 UTC are denoted by red circles. Vertical vorticity at 100 m AGL (dark green contours) is contoured at intervals of $(-2.5, 2.5, 5, 10) \times 10^{-3}\ \mathrm{s}^{-1}$ in (a) and $(5, 10, 15, 20, 30, 40) \times 10^{-3}\ \mathrm{s}^{-1}$ in (b). Ground-relative wind speeds at 100 m AGL are shown as magenta isolines. Thick black lines denote the trajectories of rear-inflow (P1 and P2) and prefrontal-inflow (P3) parcels examined in Figs. 17–19. Tick marks are spaced 0.8 km apart.

stretching (Fig. 19b). Indeed, negative stretching is found for the horizontal vorticity. As noted in Davies-Jones and Markowski (2013), inflow parcel is decelerated in a strong adverse pressure gradient when approaching the gust front, which consequently results in a compression of its horizontal vorticity. In addition, since P3 spends a long time in the prefrontal homogeneous region, baroclinicity only plays a minor role in the production of horizontal vorticity. The conversion between streamwise and crosswise vorticity is also weak. It occurs as P3 terminates on the outer periphery of MVa, following a quasi-straight trajectory (Fig. 15). Little change is found in the horizontal wind direction of P3, except when it approaches MVa at the gust front. For parcels that enter the mesovortex and ascend spirally, significant conversion between crosswise and streamwise vorticity will take place, as shown in Mashiko et al. (2009) and Schenkman et al. (2014).

7. Further discussions

The above analyses show that both the circulations associated with MVa and MVb experience a rapid increase in the last few minutes prior to mesovortex genesis. At such late stage, the material circuit has descended to a low level near the surface, either with the system RIJ or convective-scale downdrafts. Surface friction is found to play a notable role in generating circulation for these low-level MVs at 100 m AGL. However, circulation analyses at higher levels (e.g., 1 km AGL) reveal a much weaker impact of friction (not shown). This is reasonable because the frictional contribution is mainly limited to the lowest ~(200–300) m above the ground (Figs. 12 and 15). The decrease of frictional effect with height can also be inferred from Fig. 9. The horizontal vorticity aloft are much smaller than near the surface. More importantly, the horizontal vorticity there is oriented in a direction consistent with baroclinic generation.

Baroclinicity has long been recognized to be the main contributor to the intensification of low-level circulations (e.g., Rotunno and Klemp 1985; Atkins and St. Laurent 2009b). This study suggests that surface friction may be another important contributor to the intensification of low-level MVs. This does not rule out the importance of baroclinicity, however. For example, the circulation about CirB grows via baroclinic generation before 1423 UTC; the positive contribution of friction after 1422 UTC is largely offset by its negative contribution before, leading to a net small frictional generation of circulation (Fig. 10d). The two circuits CirA and CirB are tracked backward into the convective system for 12 min, which only accounts for part of the rear-inflow parcels' journey in the convective system. Considerable circulations are found at the "beginning" time of

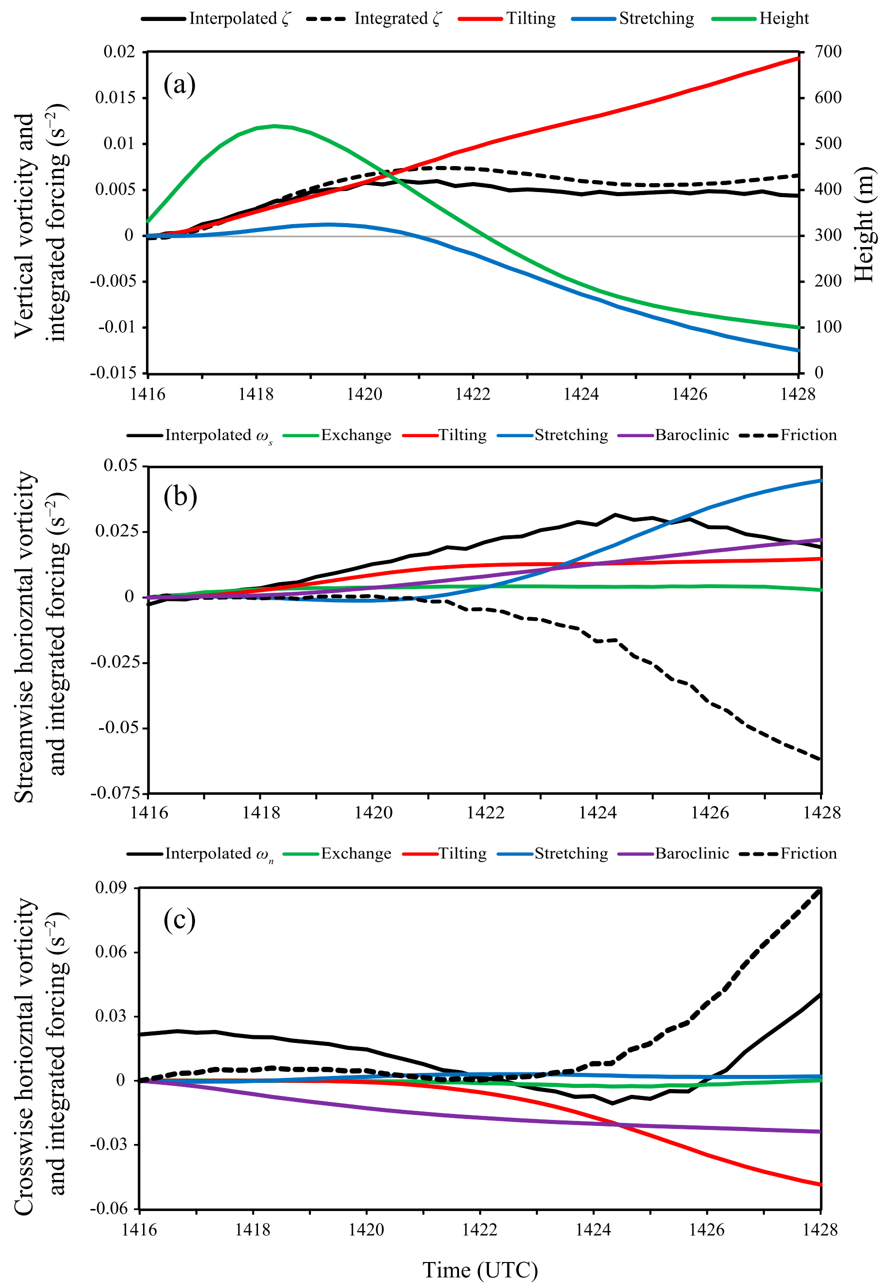

FIG. 17. Vorticity budgets for the rear-inflow parcel P1 on CirB during 1416–1428 UTC. (a) Vertical vorticity, and (b) streamwise and (c) crosswise horizontal vorticity. Trajectory of P1 is shown in Fig. 16a.

both circuits (i.e., 1416 and 1436 UTC, Figs. 10c and 13c). These ‘‘initial’’ circulations are predominantly distributed in the circuits' rear-flank portion behind the gust front (not shown), which seemingly are created via baroclinicity at even earlier times. The vertical vorticity of MVs was believed to have originated from the reorientation of storm-generated (i.e., baroclinic) horizontal vorticity that was tilted by either downdrafts (Trapp and Weisman 2003) or updrafts (Atkins and St. Laurent 2009b). Similar results were found for tornadoes (e.g., Markowski et al. 2008) while downward tilting was shown to be more preferable for the genesis of near-surface rotation (Davies-Jones and Markowski 2013). In this study, vorticity budgets reveal the importance of a frictional instead of baroclinic generation of horizontal vorticity near the surface, which is consistent with Schenkman et al. (2014) for tornadogenesis. However, the weak baroclinic generation for rear-inflow

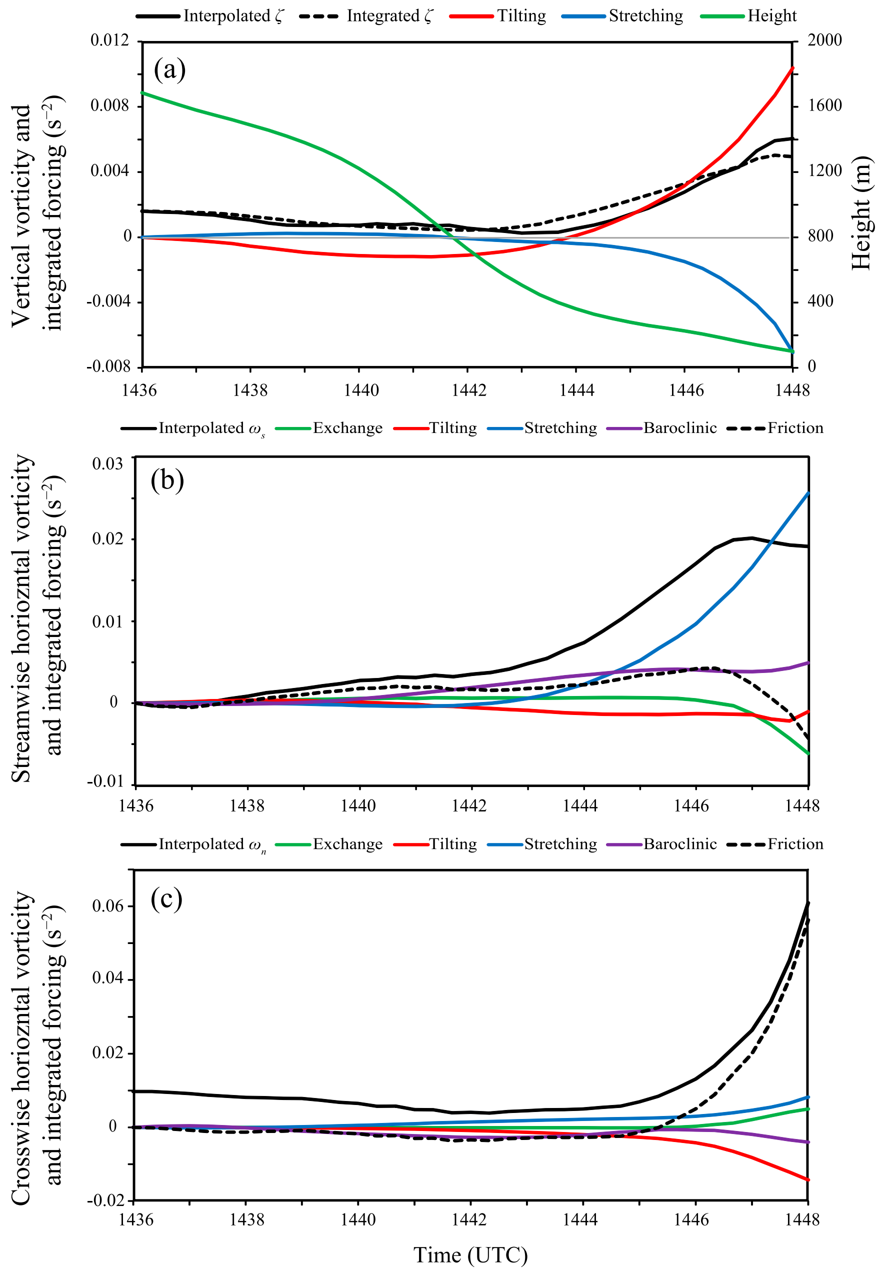

FIG. 18. As in Fig. 17 but for the rear-inflow parcel P2 on CirA during 1436–1448 UTC. Trajectory of P2 is shown in Fig. 16b.

parcels might be due to the relatively short backward-tracking time. If these parcels were tracked backward into the convective system for a longer time, they would be expected to experience more baroclinic generation of horizontal vorticity.

Although both MVa and MVb similarly show a frictional generation of circulation and horizontal vorticity, MVa finally develops into an intense mesovortex while MVb remains weak. The intensification of MVa is schematically described in a conceptual model (Fig. 20). The MV is located near the bow apex, on the south flank of the system RIJ. As the RIJ descends, an intense downdraft extending to the ground develops behind the MV (i.e., on its western side). The descending RIJ produces a low-level outflow that is generally directed toward south behind the MV. Because of the influence of surface friction, eastward horizontal vorticity is generated by the southward outflow. From the viewpoint of circulation, the eastward horizontal vorticity penetrates the tilted material surface enclosing the MV and

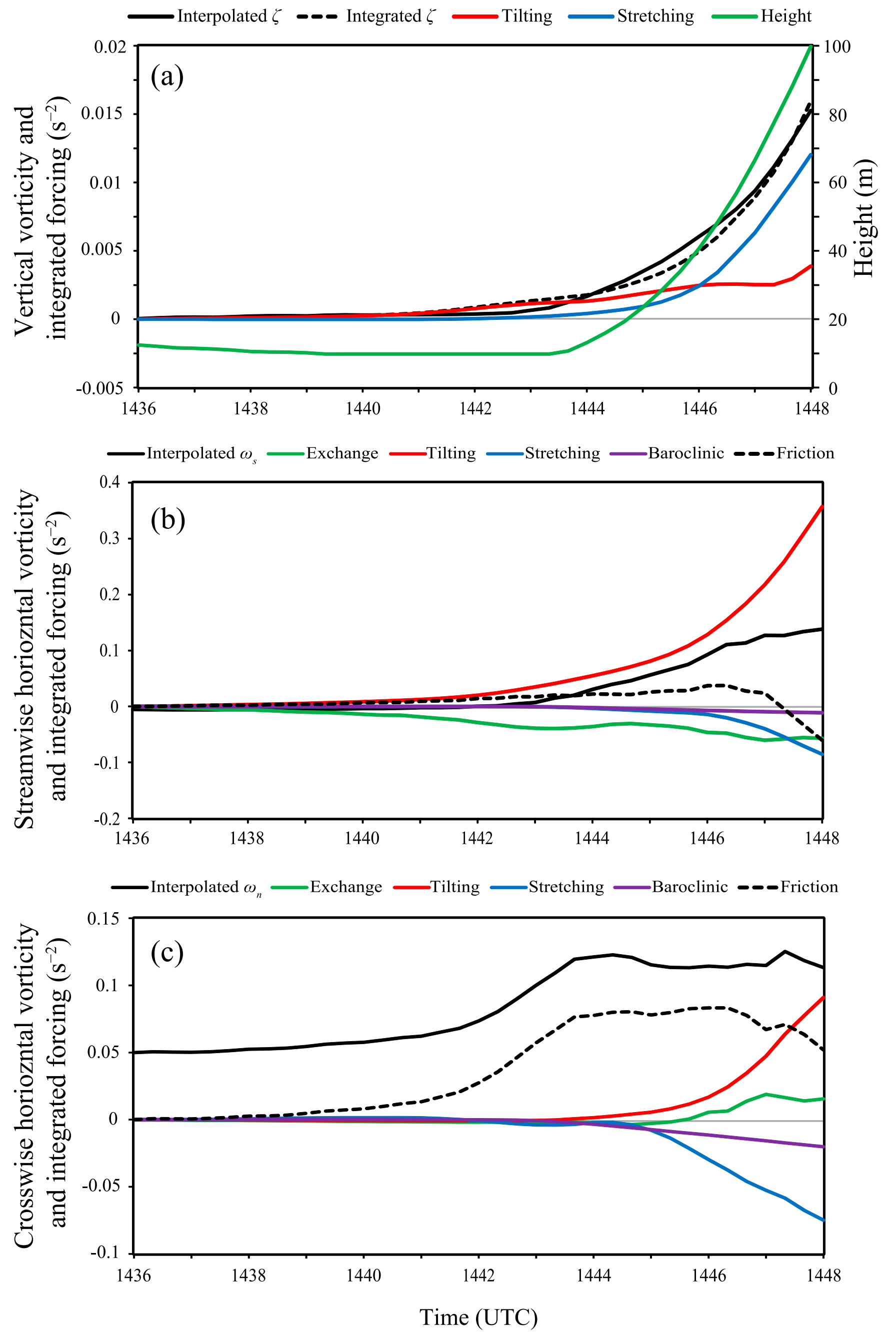

FIG. 19. As in Fig. 17 except for the prefrontal-inflow parcel P3 on CirA during 1436–1448 UTC. Trajectory of P3 is shown in Fig. 16b.

consequently increases the circulation about this circuit. The rotation of the MV is further enhanced and the vortex intensifies into a strong mesovortex by the shrinking of the material circuit, which occurs in response to the great convergence promoted by the intense rear-side downdraft. From the viewpoint of vorticity, the frictionally induced horizontal vortex tube is tilted into vertical and then stretched into an intense mesovortex by the strong horizontal convergence. This is quite different from the tilting generation mechanisms of MVs proposed in previous idealized numerical studies. For one thing, the tilted horizontal vorticity in our conceptual model primarily originates from surface friction instead of baroclinicity. For another, the resultant horizontal vorticity is largely normal to the gust front. Therefore, it can be effectively tilted by the sharp gradient of vertical velocity

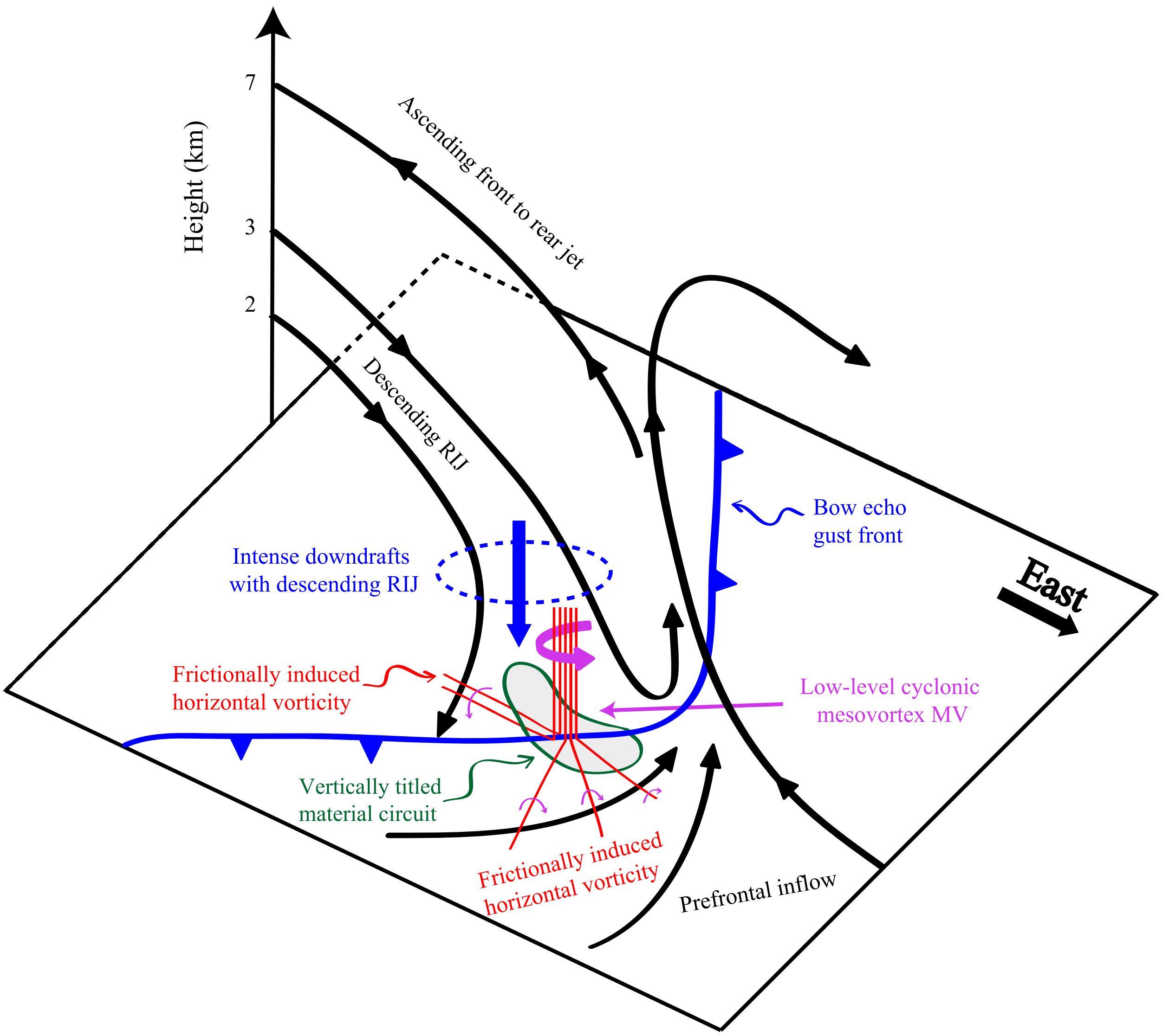

FIG. 20. Schematic showing the genesis of the strong mesovortex MV near the apex of a large bow echo. The bow echo gust front is marked in blue line with triangles. The prefrontal inflow, ascending front to rear jet, and descending rear-inflow jet (RIJ) are all depicted in black lines with arrows. Red lines denote the vortex lines, with their rotations indicated by the purple curve arrows surrounding them. MV is located in the position where the vortex lines are erect. The material circuit enclosing MV is colored in green with gray shading. The downward-directed blue arrow denotes the intense downdrafts behind MV, which are associated with the descending RIJ and extend well down to the surface. This schematic shows the stage a few minutes prior to mesovortex genesis.

between downdrafts and updrafts at the gust front. In contrast, baroclinicity generally creates a horizontal vorticity parallel to the gust front, which has to be tilted into the vertical by localized downdrafts or updrafts along the gust front.

8. Summary and conclusions

A real-data, convection-resolving simulation is performed using the ARW model for a severe bow echo system that occurred over the central United States on 8 May 2009. The model domain is configured with a pair of two-way nested grids having 4- and 0.8-km grid spacings, respectively. The simulated bow echo generally agrees well with observations, with a number of mesovortices (MVs) produced along the system's leading convective line. Two MVs (MVa and MVb) that formed near the bow apex in the simulation are studied, which differ distinctively in intensity, lifetime, and damage potential.

MVa persists for over 2 h and remains close to the bow apex, embedded within the system's rear-inflow jet (RIJ). Strong downdrafts are produced behind MVa owing to the descent of the RIJ, which significantly enhances the low-level convergence near the gust front and in turn causes strong stretching of vertical vorticity. Moreover, a sharp gradient of vertical velocity is created by the downdraft–updraft couplets at the gust front, which efficiently tilt the horizontal vorticity into vertical. MVa finally develops into an intense mesovortex, reaching high vertical vorticity values of up to $0.053\,s^{-1}$ at 100 m AGL. Strong winds of over $50\,m\,s^{-1}$ are found in association with MVa near the surface. In contrast, MVb is nondamaging and shorter lived. It lasts for about 1 h, moving away from the bow apex over time. MVb is accompanied with convective-scale downdrafts and experiences much weaker stretching and tilting. Therefore, it only develops a peak vertical vorticity of about $0.012\,s^{-1}$ at 100 m AGL.

Circulations about the material circuits enclosing MVa and MVb are analyzed. The results show that air parcels on the circuits originate from both ahead of (i.e., prefrontal inflow) and behind (i.e., rear inflow) the gust front. The rear-inflow parcels descend with time and finally converge with the ascending prefrontal-inflow parcels at the gust front. As a result, the area enclosed by the circuit shrinks markedly. For MVa, the descending parcels subside with the system RIJ from higher altitudes of up to 2 km AGL, while for MVb they descend with the localized downdrafts from a lower level at around 500–600 m AGL. Budgets of circulation show that, in addition to baroclinicity, friction can also contribute to the production of near-surface rotation, especially during the final few minutes prior to mesovortex genesis. This occurs as the frictionally generated horizontal vortex tubes pass through the tilted material circuit surface.

The influence of friction is confirmed by examining the near-surface horizontal vorticity. At low levels, the horizontal vorticity are generally crosswise, oriented in a direction opposite to baroclinically generated vorticity even at the gust front. Lagrangian vorticity budget analyses show that such crosswise vorticity is primarily generated by surface friction. The descending rear-inflow parcels acquire their vertical vorticity through the tilting of horizontal vorticity. On the contrary, for the prefrontal-inflow parcels, the increase in vertical vorticity is predominantly accounted for by vertical stretching at the gust front. However, tilting still plays a role in that it provides the initial vertical vorticity for subsequent stretching. To conclude, the influence of friction should be taken into account when studying the genesis of low-level MVs within quasi-linear convective systems (QCLSs). Reorientation of frictionally generated horizontal vorticity can make a notable contribution to the development of near-surface vertical rotation. In fact, the need to consider surface friction and the contribution of surface-friction-generated vorticity is also pointed out in recent tornadogenesis studies (Schenkman et al. 2012, 2014).

The conclusions drawn in this paper are based on the numerical simulation of a single case. The MVs and their parent system, the 8 May 2009 bow echo, formed in an environment with given conditions. Previous studies have suggested notable dependency on the vertical wind shear and ambient CAPE for the development of MVs (Weisman and Trapp 2003; Atkins and St. Laurent 2009a). Moreover, the simulation performed is based on specific experiment setup. Substantial variations were noticed for the evolution of the large bow echo when changing the model physics, initial, and boundary conditions during the CAPS SSEFs (Xue et al. 2009). Clearly, more cases and simulations should be studied to obtain more robust and general conclusions on the genesis of low-level MVs within QCLSs.

Acknowledgments. This work was primarily supported by the National 973 Fundamental Research Program of China (2013CB430103). Xin Xu was supported by the Chinese Scholarship Council for his extended visit at the Center for Analysis and Prediction of Storms, University of Oklahoma. The second author acknowledges the support of the National Thousand Person Plan hosted at the Nanjing University and the support of NSF Grants AGS-0802888, OCI-0905040, AGS-0941491, AGS-1046171, and AGS-1046081. Initial conversations with Dr. Michael Coniglio focused our attention to the mesovortices within this bow echo case.

REFERENCES

Adlerman, E. J., K. K. Droegemeier, and R. P. Davies-Jones, 1999: A numerical simulation of cyclic mesocyclogenesis. *J. Atmos. Sci.,* **56,** 2045–2069, doi:10.1175/1520-0469(1999)056<2045:ANSOCM>2.0.CO;2.

Atkins, N. T., and M. St. Laurent, 2009a: Bow echo mesovortices. Part I: Processes that influence their damaging potential. *Mon. Wea. Rev.,* **137,** 1497–1513, doi:10.1175/2008MWR2649.1.

——, and ——, 2009b: Bow echo mesovortices. Part II: Their genesis. *Mon. Wea. Rev.,* **137,** 1514–1532, doi:10.1175/2008MWR2650.1.

——, J. M. Arnott, R. W. Przybylinski, R. A. Wolf, and B. D. Ketcham, 2004: Vortex structure and evolution within bow echoes. Part I: Single-Doppler and damage analysis of the 29 June 1998 derecho. *Mon. Wea. Rev.,* **132,** 2224–2242, doi:10.1175/1520-0493(2004)132<2224:VSAEWB>2.0.CO;2.

——, C. S. Bouchard, R. W. Przybylinski, R. J. Trapp, and G. Schmocker, 2005: Damaging surface wind mechanism within the 10 June 2003 Saint Louis bow echo during BAMEX. *Mon. Wea. Rev.,* **133,** 2275–2296, doi:10.1175/MWR2973.1.

Coniglio, M. C., S. F. Corfidi, and J. S. Kain, 2011: Environment and early evolution of the 8 May 2009 derecho-producing convective system. *Mon. Wea. Rev.,* **139,** 1083–1102, doi:10.1175/2010MWR3413.1.

Davies-Jones, R. P., 1982a: A new look at the vorticity equation with application to tornadogenesis. Preprints, *12th Conf. on Severe Local Storms,* San Antonio, TX, Amer. Meteor. Soc., 249–252.

——, 1982b: Observational and theoretical aspects of tornadogenesis. *Intense Atmospheric Vortices,* L. Bengtsson and J. Lighthill, Eds., Springer-Verlag, 175–189.

——, and H. E. Brooks, 1993: Mesocyclogenesis from a theoretical perspective. *The Tornado: Its Structure, Dynamics, Prediction, and Hazards, Geophys. Monogr.,* Vol. 79, Amer. Geophys. Union, 105−114.

——, and P. M. Markowski, 2013: Lifting of ambient air by density currents in sheared environments. *J. Atmos. Sci.,* **70,** 1204–1215, doi:10.1175/JAS-D-12-0149.1.

Doswell, C. A., III, H. H. Brooks, and N. Dotzek, 2009: On the implementation of the enhanced Fujita scale in the USA. *Atmos. Res.,* **93,** 554–563, doi:10.1016/j.atmosres.2008.11.003.

Ek, M. B., K. E. Mitchell, Y. Lin, E. Rogers, P. Grunmann, V. Koren, G. Gayno, and J. D. Tarpley, 2003: Implementation of Noah land surface model advances in the National Centers for Environmental Prediction operational mesoscale Eta model. *J. Geophys. Res.,* **108,** 8851, doi:10.1029/2002JD003296.

Evans, C., M. L. Weisman, and L. F. Bosart, 2014: Development of an intense, warm-core mesoscale vortex associated with the 8 May 2009 ''super derecho'' convective event. *J. Atmos. Sci.,* **71,** 1218–1240, doi:10.1175/JAS-D-13-0167.1.

Forbes, G. S., and R. M. Wakimoto, 1983: A concentrated outbreak of tornadoes, downbursts and microbursts, and implications regarding vortex classification. *Mon. Wea. Rev.,* **111,** 220–235, doi:10.1175/1520-0493(1983)111<0220:ACOOTD>2.0.CO;2.

Fujita, T. T., 1981: Tornadoes and downbursts in the context of generalized planetary scales. *J. Atmos. Sci.,* **38,** 1511–1534, doi:10.1175/1520-0469(1981)038<1511:TADITC>2.0.CO;2.

Funk, T. W., K. E. Darmofal, J. D. Kirkpatrick, V. L. Dewald, R. W. Przybylinski, G. K. Schmocker, and Y.-J. Lin, 1999: Storm reflectivity and mesocyclone evolution associated with the 15 April 1994 squall line over Kentucky and southern Indiana. *Wea. Forecasting,* **14,** 976–993, doi:10.1175/1520-0434(1999)014<0976:SRAMEA>2.0.CO;2.

Gao, J., M. Xue, K. Brewster, and K. K. Droegemeier, 2004: A three-dimensional variational data analysis method with recursive filter for Doppler radars. *J. Atmos. Oceanic Technol.,* **21,** 457–469, doi:10.1175/1520-0426(2004)021<0457:ATVDAM>2.0.CO;2.

Grzych, M. L., B. D. Lee, and C. A. Finley, 2007: Thermodynamic analysis of supercell rear-flank downdrafts from project ANSWERS. *Mon. Wea. Rev.,* **135,** 240–246, doi:10.1175/MWR3288.1.

Houze, R. A., Jr., 2004: Mesoscale convetive systems. *Rev. Geophys.,* **42,** RG4003, doi:10.1029/2004RG000150.

Janjić, Z. I., 1994: The step-mountain Eta coordinate model: Further developments of the convection, viscous sublayer, and turbulence closure schemes. *Mon. Wea. Rev.,* **122,** 927–945, doi:10.1175/1520-0493(1994)122<0927:TSMECM>2.0.CO;2.

——, 1996: The surface layer in the NCEP Eta Model. Preprints, *11th Conf. on Numerical Weather Prediction,* Norfolk, VA, Amer. Meteor. Soc., 354–355.

Johns, R. H., and W. D. Hirt, 1987: Derechos: Widespread convectively induced wind-storms. *Wea. Forecasting,* **2,** 32–49, doi:10.1175/1520-0434(1987)002<0032:DWCIW>2.0.CO;2.

Kong, F., and Coauthors, 2009: A real-time storm-scale ensemble forecast system: 2009 Spring Experiment. Preprints, *23rd Conf. on Weather Analysis and Forecasting/19th Conf. on Numerical Weather Prediction,* Omaha, NE, Amer. Meteor. Soc., 16A.3. [Available online at https://ams.confex.com/ams/23WAF19NWP/techprogram/paper_154118.htm.]

Kosiba, K., J. Wurman, Y. P. Richardson, P. M. Markowski, P. Robinson, and J. N. Marquis, 2013: Genesis of the Goshen County, Wyoming, Tornado on 5 June 2009 during VORTEX2. *Mon. Wea. Rev.,* **141,** 1157–1181, doi:10.1175/MWR-D-12-00056.1.

Lee, B. D., C. A. Finley, and C. D. Karstens, 2012: The Bowdle, South Dakota, cyclic tornadic supercell of 22 May 2012: Surface analysis of rear-flank downdraft evolution and multiple internal surges. *Mon. Wea. Rev.,* **140,** 3419–3441, doi:10.1175/MWR-D-11-00351.1.

Lemon, L. R., and C. A. Doswell, 1979: Severe thunderstorms evolution and mesocyclone structure as related to tornadogenesis. *Mon. Wea. Rev.,* **107,** 1184–1197, doi:10.1175/1520-0493(1979)107<1184:STEAMS>2.0.CO;2.

Lilly, D. K., 1982: The development and maintenance of rotation in convective storms. *Intense Atmospheric Vortices,* L. Bengtsson and J. Lighthill, Eds., Springer-Verlag, 149–160.

Markowski, P. M., 2002: Hook echoes and rear-flank downdrafts: A review. *Mon. Wea. Rev.,* **130,** 852–876, doi:10.1175/1520-0493(2002)130<0852:HEARFD>2.0.CO;2.

——, J. M. Straka, and E. N. Rasmussen, 2002: Direct surface thermodynamic observations within the rear-flank downdrafts of nontornadic and tornadic supercells. *Mon. Wea. Rev.,* **130,** 1692–1721, doi:10.1175/1520-0493(2002)130<1692:DSTOWT>2.0.CO;2.

——, E. N. Rasmussen, J. M. Straka, R. P. Davies-Jones, Y. P. Richardson, and R. J. Trapp, 2008: Vortex lines within low-level mesocyclones obtained from pseudo-dual-Doppler radar observations. *Mon. Wea. Rev.,* **136,** 3513–3535, doi:10.1175/2008MWR2315.1.

Markowski, P. M, and Coauthors, 2012: The pretornadic phase of the Goshen County, Wyoming, supercell of 5 June 2009 intercepted by VORTEX2. Part II: Intensification of low-level rotation. *Mon. Wea. Rev.,* **140,** 2916–2938, doi:10.1175/MWR-D-11-00337.1.

Marquis, J. N., Y. P. Richardson, J. Wurman, and P. M. Markowski, 2008: Single- and dual-Doppler analysis of a tornadic vortex and surrounding storm scale flow in the Crowell, TX, supercell of 30 April 2000. *Mon. Wea. Rev.,* **136,** 5017–5043, doi:10.1175/2008MWR2442.1.

——, ——, P. M. Markowski, D. Dowell, and J. Wurman, 2012: Tornado maintenance investigated with high-resolution dual-Doppler and EnKF analysis. *Mon. Wea. Rev.,* **140,** 3–27, doi:10.1175/MWR-D-11-00025.1.

Mashiko, W., H. Niino, and K. Teruyuki, 2009: Numerical simulations of tornadogenesis in an outer-rainband minisupercell of typhoon Shanshan on 17 September 2006. *Mon. Wea. Rev.,* **137,** 4238–4260, doi:10.1175/2009MWR2959.1.

Meng, Z., F. Zhang, P. Markowski, D. Wu, and K. Zhao, 2012: A modeling study on the development of a bowing structure and associated rear inflow within a squall line over South China. *J. Atmos. Sci.,* **69,** 1182–1207, doi:10.1175/JAS-D-11-0121.1.

Orlanski, I., 1975: A rational subdivision of scales for atmospheric processes. *Bull. Amer. Meteor. Soc.,* **56,** 527–530.

Rotunno, R., and J. B. Klemp, 1985: On the rotation and propagation of simulated supercell thunderstorms. *J. Atmos. Sci.,* **42,** 271–292, doi:10.1175/1520-0469(1985)042<0271:OTRAPO>2.0.CO;2.

Schenkman, A. D., M. Xue, and A. Shapiro, 2012: Tornadogenesis in a simulated mesovortex within a mesoscale convective system. *J. Atmos. Sci.,* **69,** 3372–3390, doi:10.1175/JAS-D-12-038.1.

——, ——, and M. Hu, 2014: Tornadogenesis in a high-resolution simulation of the 8 May 2003 Oklahoma City supercell. *J. Atmos. Sci.,* **71,** 130–154, doi:10.1175/JAS-D-13-073.1.

Shabbott, C. J., and P. M. Markowski, 2006: Surface in site observations within the outflow of forward-flank downdrafts of supercell thunderstorms. *Mon. Wea. Rev.,* **134,** 1422–1441, doi:10.1175/MWR3131.1.

Skamarock, W. C., J. B. Klemp, J. Dudhia, D. O. Gill, D. M. Barker, W. Wang, and J. G. Powers, 2005: A description of the advanced research WRF version 2. NCAR Tech. Note TN-468+STR, 88 pp. [Available online at http://www.mmm.ucar.edu/wrf/users/docs/arw_v2.pdf.]

Smull, B. F., and R. A. Houze Jr., 1987: Rear inflow in squall lines with trailing stratiform precipitation. *Mon. Wea. Rev.,* **115,** 2869–2889, doi:10.1175/1520-0493(1987)115<2869:RIISLW>2.0.CO;2.

Tao, W.-K., and Coauthors, 2003: Microphysics, radiation, and surface processes in the Goddard Cumulus Ensemble (GCE) model. *Meteor. Atmos. Phys.,* **82,** 97–137, doi:10.1007/s00703-001-0594-7.

Thompson, G., P. R. Field, R. M. Rasmussen, and W. D. Hall, 2008: Explicit forecasts of winter precipitation using an improved bulk microphysics scheme. Part II: Implementation of a new snow parameterization. *Mon. Wea. Rev.,* **136,** 5095–5115, doi:10.1175/2008MWR2387.1.

Trapp, R. J., and M. L. Weisman, 2003: Low-level mesovortices within squall lines and bow echoes. Part II: Their genesis and implications. *Mon. Wea. Rev.,* **131,** 2804–2823, doi:10.1175/1520-0493(2003)131<2804:LMWSLA>2.0.CO;2.

Trier, S. B., W. C. Skamarock, and M. A. LeMone, 1997: Structure and evolution of the 22 February 1993 TOGA COARE squall line: Organization mechanisms inferred from numerical simulation. *J. Atmos. Sci.,* **54,** 386–407, doi:10.1175/1520-0469(1997)054<0386:SAEOTF>2.0.CO;2.

Wakimoto, R. M., H. V. Murphey, A. Nester, D. P. Jorgensen, and N. T. Atkins, 2006a: High winds generated by bow echoes. Part I: Overview of the Omaha bow echo 5 July 2003 storm during BAMEX. *Mon. Wea. Rev.,* **134,** 2793–2812, doi:10.1175/MWR3215.1.

——, ——, C. A. Davis, and N. T. Atkins, 2006b: High winds generated by bow echoes. Part II: The relationship between the mesovortices and damaging straight-line winds. *Mon. Wea. Rev.,* **134,** 2813–2829, doi:10.1175/MWR3216.1.

Walko, R. L., 1993: Tornado spin-up beneath a convective cell: Required basic structure of the near-field boundary layer winds. *The Tornado: Its Structure, Dynamics, Prediction, and Hazards, Geophys. Monogr.,* Vol. 79, Amer. Geophys. Union, 89–95.

Weisman, M. L., and C. A. Davis, 1998: Mechanisms for the generation of mesoscale vortices within quasi-linear convective systems. *J. Atmos. Sci.,* **55,** 2603–2622, doi:10.1175/1520-0469(1998)055<2603:MFTGOM>2.0.CO;2.

——, and R. J. Trapp, 2003: Low-level mesovortices within squall lines and bow echoes. Part I: Overview and sensitivity to environmental vertical wind shear. *Mon. Wea. Rev.,* **131,** 2779–2803, doi:10.1175/1520-0493(2003)131<2779:LMWSLA>2.0.CO;2.

——, C. Evans, and L. Bosart, 2013: The 8 May 2009 superderecho: Analysis of a real-time explicit convective forecast. *Wea. Forecasting,* **28,** 863–892, doi:10.1175/WAF-D-12-00023.1.

Wheatley, D. M., and R. J. Trapp, 2008: The effect of mesoscale heterogeneity on the genesis and structure of mesovortices within quasi-linear convective systems. *Mon. Wea. Rev.,* **136,** 4220–4241, doi:10.1175/2008MWR2294.1.

——, ——, and N. T. Atkins, 2006: Radar and damage analysis of severe bow echoes observed during BAMEX. *Mon. Wea. Rev.,* **134,** 791–806, doi:10.1175/MWR3100.1.

Xu, X., M. Xue, and Y. Wang, 2015: Mesovortices within the 8 May 2009 bow echo over central United States: Analyses of the characteristics and evolution based on Doppler radar observations and a high-resolution model simulation. *Mon. Wea. Rev.,* doi:10.1175/MWR-D-14-00234.1, in press.

Xue, M., K. K. Droegemeier, and V. Wong, 2000: The Advanced Regional Prediction System (ARPS)—A multi-scale nonhydrostatic atmospheric simulation and prediction model. Part I: Model dynamics and verification. *Meteor. Atmos. Phys.,* **75,** 161–193, doi:10.1007/s007030070003.

——, D.-H. Wang, J.-D. Gao, K. Brewster, and K. K. Droegemeier, 2003: The Advanced Regional Prediction System (ARPS), storm-scale numerical weather prediction and data assimilation. *Meteor. Atmos. Phys.,* **82,** 139–170, doi:10.1007/s00703-001-0595-6.

——, and Coauthors, 2009: CAPS realtime 4-km multi-model convection-allowing ensemble and 1-km convection-resolving forecasts for the NOAA Hazardous Weather Testbed 2009 Spring Experiment. Preprints, *23rd Conf. on Weather Analysis and Forecasting/19th Conf. on Numerical Weather Prediction,* Omaha, NE, Amer. Meteor. Soc., 16A.2. [Available online at https://ams.confex.com/ams/23WAF19NWP/techprogram/paper_154323.htm.]